nature communications

Article

https://doi.org/10.1038/s41467-024-52975-2

CYpHER: catalytic extracellular targeted protein degradation with high potency and durable effect

Received: 25 March 2024

Accepted: 27 September 2024

Published online: 09 October 2024

Check for updates

Zachary R. Crook[1,2,3], Gregory P. Sevilla[1,2,3], Pamela Young[2], Emily J. Girard[4], Tinh-Doan Phi[2], Monique L. Howard[5], Jason Price[3], James M. Olson[3,4] & Natalie W. Nairn[1,2]

Many disease-causing proteins have multiple pathogenic mechanisms, and conventional inhibitors struggle to reliably disrupt more than one. Targeted protein degradation (TPD) can eliminate the protein, and thus all its functions, by directing a cell's protein turnover machinery towards it. Two established strategies either engage catalytic E3 ligases or drive uptake towards the endolysosomal pathway. Here we describe CYpHER (**C**atal**Y**tic **pH**-dependent **E**ndolysosomal delivery with **R**ecycling) technology with potency and durability from a catalytic mechanism that shares the specificity and straightforward modular design of endolysosomal uptake. By bestowing pH-dependent release on the target engager and using the rapid-cycling transferrin receptor as the uptake receptor, CYpHER induces endolysosomal delivery of surface and extracellular targets while re-using drug, potentially yielding increased potency and reduced off-target tissue exposure risks. The TfR-based approach allows targeting to tumors that overexpress this receptor and offers the potential for transport to the CNS. CYpHER function was demonstrated in vitro with EGFR and PD-L1, and in vivo with EGFR in a model of EGFR-driven non-small cell lung cancer.

Contemporary targeted therapeutics aim to modulate the activity of a particular target, usually a protein, that has a defined role in disease pathology. This modulation is often the disruption of protein function, most commonly seen by enzyme inhibition (e.g., kinase inhibitors) or steric blocking (e.g., antibodies). These conventional inhibitors and blockers can disrupt a defined function, and often add beneficial pleiotropic effects, such as protein homeostasis disruption[1] or altered target trafficking[2,3]. Nevertheless, these drugs are often insufficient to meaningfully and durably alter disease pathology. For one, many targets exhibit multiple functions, and inhibiting one function can leave the others available for potentiating pathologic signaling. Second, the nature of many of these inhibitors leaves them particularly vulnerable to cellular adaptation and mutational resistance that diminishes drug durability.

An exemplary group of protein targets is receptor tyrosine kinases (RTKs) in cancer, as they can potentiate growth, differentiation, and survival signaling[4]. Many involve a mechanism for activation that involves multimerization and cross-phosphorylation at the cell surface. As such, they not only function as kinases, but as kinase substrates mediating signal transduction. Tyrosine kinase inhibitors (TKIs) and antibodies are typical RTK-targeted therapeutics. TKIs can disrupt kinase activity of RTKs[5], but they do not block the RTKs from being substrates for other kinases. As many RTKs function through both homo- and heterodimerization with other RTKs, this leads to resistance via upregulation of other partners[6]. As an additional liability, point mutations can often directly or indirectly disrupt TKI binding[7]. Conversely, antibodies can alter the multimerization tendencies of

[1]Cyclera Therapeutics Inc, Seattle, WA 98115, USA. [2]Blaze Bioscience Inc, Seattle, WA 98109, USA. [3]Clinical Research Division, Fred Hutchinson Research Center, Seattle, WA 98109, USA. [4]Ben Towne Center for Childhood Cancer Research, Seattle Children's Research Institute, Seattle, WA 98105, USA. [5]NW Biosensor, Seattle, WA 98103, USA. e-mail: natalie.nairn@cycleratx.com

RTKs, but with kinase function retained, target or heterodimer partner upregulation (or gain-of-function mutation) becomes a common resistance mechanism[8], with increased total membrane kinase activity compensating for disrupted multimerization. Altogether, these inhibitors can be effective for a period of time, but the myriad mechanisms for functional bypass typically render their efficacy transient.

In order to simultaneously disrupt all of a target's disease-associated functions, targeted protein degradation (TPD) can be used. Expertly summarized in a recent review[9], TPD leverages cells' mechanisms for target turnover, altering the kinetics of this process for specific targets. This is mainly through formation of ternary complexes between target protein and degradation effector. For intracellular (e.g., molecular glue and PROTAC)[10] and some extracellular (e.g., AbTAC and REULR)[11,12] molecules, this is through E3 ligase recruitment, inducing ubiquitin-mediated target degradation by the proteasome or lysosome. This benefits from a catalytic mechanism of action (the drug is not expended in the process) but can be complicated by finding an E3 ligase expressed in the target tissue that can be induced to interact in an effective orientation with the target for functional ubiquitination. Meanwhile, small molecules (e.g., molecular glue and PROTAC) also have many of the same point mutational resistance liabilities of TKIs. Other approaches used for surface and extracellular soluble targets (e.g., LYTAC, ATAC, KineTAC)[13–15] engage surface protein trafficking systems. Often targeting membrane sugar receptors (cation-independent mannose-6-phosphate receptor [CI-M6PR] or asialoglycoprotein receptor [ASGPR]) but also cytokine receptors (e.g., CXCR7), these are designed to "hitch a ride" with the uptake receptor into the cell before target release in the endolysosomal system. These tend to be biologics, benefiting from modular design and greater target specificity, but the drug follows the target through its trafficking, limited to stoichiometric (as opposed to catalytic) activity.

Transferrin receptor (TfR) is another such uptake receptor with potential in extracellular TPD (eTPD) approaches. Its normal role is facilitating uptake of iron-loaded transferrin (holoTF)[16]. Upon uptake and endosomal maturation, which involves acidification to roughly pH 5.5, transferrin releases its iron but remains bound to TfR, returning to the surface with its receptor. The process takes ~10–20 min[16], repeating dozens to hundreds of times over the protein's lifetime[17]. Our work concerns the development of eTPD molecules that mimic the behavior of transferrin, as they are engineered for reduced binding affinity at endosomal pH to permit target release and subsequent trafficking through the endolysosomal system. They also contain a TfR-binding end with no such pH sensitivity, which permits the molecules to return to the surface to take in additional targets. This catalytic activity increases potency (multiple target molecules eliminated by a single drug), permits retained activity after drug is cleared from extracellular space, and should reduce the disruptive effects of shed, soluble variants of a membrane target (that can otherwise act as a decoy for conventional antibodies)[18], since the soluble form would simply represent one round of uptake and endosomal release.

Using TfR as the uptake receptor presents numerous advantages, particularly for CNS disease and oncology. TfR is commonly upregulated on a wide variety of solid tumors[19,20], presumably to accommodate the increased iron demands in rapidly-dividing cells, and its overexpression often correlates with disease severity[20,21]. This overexpression compared to healthy tissue should concentrate the drug in the tumor tissue, improving the therapeutic window. Also, cancer cells are highly dependent on TfR for growth[22], so a potential resistance mechanism of receptor downregulation is avoided by using TfR. In addition, TfR is well known as a mediator of blood-brain barrier transcytosis[23], having been used to deliver biologic molecules to the brain parenchyma[24,25]. A drug whose mechanism of action includes TfR engagement has the potential to enable specific depletion of targets in the CNS, an area of high unmet medical need. We note that, during the preparation of this work, another group also highlighted the advantages of TfR-based TPD for oncology (TransTACs)[26], but designed the molecules to be degraded in the endosome to avoid (rather than harness) TfR-based recycling for catalytic activity.

Here, we present CYpHER (**C**atal**Y**tic **pH**-dependent **E**ndolysosomal delivery with **R**ecycling), an eTPD technology that combines the specificity and modularity of an endolysosomal trafficking approach with a catalytic mechanism. We demonstrate the development of CYpHER molecules, catalytic target uptake and elimination, suppressing signaling and growth of cancer cells, and in vivo pharmacokinetics and activity. We discuss the steps for engineering molecules with these characteristics, assays for demonstrating surface target elimination and uptake of multiple targets per drug molecule, and then discuss potential advantages and utilities of this approach.

Results

The CYpHER concept

The core CYpHER concept is illustrated in Fig. 1a, b. A simplistic diagram of a CYpHER molecule (Fig. 1a) includes a pH-dependent target-binder linked to a recycling uptake receptor-binder (here, a TfR binder). After CYpHER has initiated ternary complex formation on the cell surface (Fig. 1b), the target and CYpHER molecule are brought into the cell in TfR-containing clathrin-coated vesicles. Following the trafficking of TfR, the vesicle then joins endosomes that begin acidifying[16]. The target-binders are engineered to release the target at low pH, permitting the TfR:CYpHER complex to be trafficked back to the surface where the target-binding end of CYpHER is free to bind and traffic additional target molecules. Meanwhile, the released target undergoes intracellular trafficking which includes lysosomal delivery and subsequent degradation.

To construct CYpHER molecules, we began with two cystine-dense peptide (CDP) miniproteins that we've recently characterized separately for other in vivo functionalities[25,27]. CDPs are of interest for incorporating into multifunctional biologics due to their small size, potential for high affinity, and high inherent protease-resistance[28]. We made use of a TfR-binding CDP allelic series[25] that maintains binding at reduced pH (Fig. 1c), has murine cross-reactivity (Fig. 1d), and has demonstrated access to the CNS[25]. Then we further engineered a PD-L1-binding CDP[27] for enhanced pH-dependent release by generating a library of variants that each contained up to two histidine substitutions, and surface-display screened to enrich for variants that conferred strong PD-L1 binding at pH 7.4 but reduced PD-L1 binding after a low-pH rinse (Fig. 1e). Three singleton histidine substitutions were significantly enriched, and when testing them as singletons and combinations, one combination (His Sub 1 + 3) was found to confer PD-L1-binding almost as well as the parental variant at pH 7.4 but conferred substantially less PD-L1 binding after a low-pH rinse (Fig. 1f). A pilot molecule comprised of the pH-dependent PD-L1-binding CDP fused via flexible Gly-Ser linker to a high affinity TfR-binding CDP (Supplementary Fig. 1A) was used to stain 293T cells transfected with PD-L1-GFP and TfR-RFP (or with TfR-RFP alone). Subsequent cell staining for a 6xHis tag on the pilot molecule and gating for double negative, GFP+/RFP−, GFP−/RFP+, or GFP+/RFP+ cells indicated increased cell staining when one or the other surface binding partner is overexpressed with a massive increase in cell staining when both are overexpressed (24–42× vs one or the other) (Supplementary Fig. 1B), confirming cooperative targeting of TfR and target.

Engineering CYpHER candidates

Additional PD-L1-targeting CYpHER candidates were generated (Fig. 2a). Both candidates contained an Fc domain with a high-affinity TfR binder fused to its C-terminus by a Gly-Ser linker. One candidate (CT-4212-1) also contained an N-terminal fusion (via Gly-Ser linker) with the pH-dependent PD-L1-binding CDP, while the other candidate (CT-4212-3) used a rigid linker from human IgA to fuse the PD-L1-binding CDP to the TfR binder's C-terminus. The two designs were to test whether a given

https://doi.org/10.1038/s41467-024-52975-2

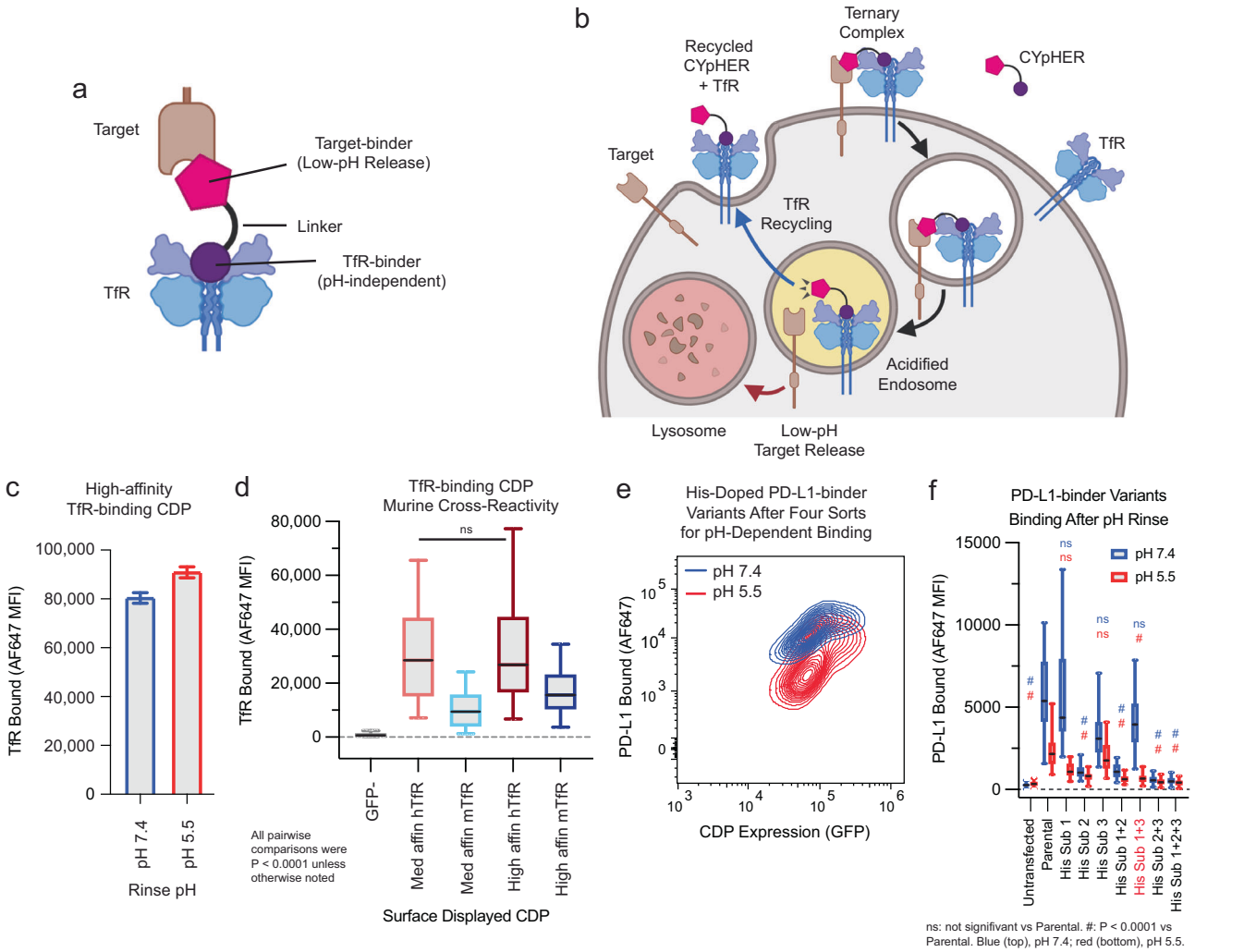

Fig. 1 | Basic principles of CYpHER and component binders. a CYpHER design including a pH-independent TfR-binding domain and a pH-dependent target-binding domain separated by a linker. **b** CYpHER mechanism. CYpHER induces ternary complex formation with target and TfR. Upon TfR-mediated uptake and endosomal acidification, target is released for endolysosomal system trafficking. TfR and CYpHER recycle to the surface for engagement with another target molecule. **c** 293F cells displaying a high-affinity TfR-binding CDP were stained with TfR and rinsed at pH 7.4 or pH 5.5 for 10 min, showing similar binding via flow cytometry in both conditions. Mean fluorescence intensity [MFI] ±95% confidence interval [CI], pH 7.4, 80.1 ± 1.9; pH 5.5, 90.6 ± 2.0; precise N per sample unavailable. **d** 293F cells displaying medium or high affinity TfR-binding CDPs were stained with human TfR (hTfR) or mouse TfR (mTfR). Kruskal–Wallis test with Dunn's correction: Med affn hTfR vs High affn hTfR was not significant ($P > 0.9999$), all others $P < 0.0001$. N cells per sample: GFP-, 479; Med affn hTfR, 317; Med affn mTfR, 295; High affn hTfR, 266; High affn mTfR, 236. **e** pH-dependent PD-L1 binding flow profile of 293F cells displaying a pool of histidine-doped variants of a PD-L1-binding CDP after four rounds of flow sorting; two for high binding after pH 7.4 rinse, two for low binding after pH 5.5 rinse. pH 7.4, $N = 38{,}979$ cells; pH 5.5, $N = 37{,}450$ cells. **f** Three His substitutions were tested as singletons and combinations for PD-L1-binding on 293F cells displaying a given binder after 10 min pH 7.4 or pH 5.5 rinse followed by flow cytometry quantitation. N cells per sample: Untransfected [UTF] 7.4, 19727; UTF 5.5, 17843; Parental 7.4, 41; Parental 5.5, 46; His sub 1 [HS1], 7.4, 27; HS1 5.5, 17; HS2 7.4, 29; HS2 5.5, 25; HS3 7.4, 58; HS3 5.5, 62; HS1 + 2 7.4, 62; HS1 + 2 5.5, 58; HS1 + 3 7.4, 25; HS1 + 3 5.5, 29; HS2 + 3 7.4, 45; HS2 + 3 5.5, 40; HS1 + 2 + 3 7.4, 87; HS1 + 2 + 3 5.5, 92. Non-Parental samples within a given pH (7.4 or 5.5) vs Parental sample by Kruskal–Wallis test with Dunn's correction: at pH 7.4, His sub 1 ($P > 0.9999$), His sub 3 ($P = 0.1161$), and His sub 1 + 3 ($P > 0.9999$) were not significant, all others $P < 0.0001$. At pH 5.5, His sub 1 ($P = 0.1666$) and His sub 3 ($P > 0.9999$) were not significant, all others $P < 0.0001$. Variant with His substitutions 1 and 3 was chosen for further work. Each experiment in **c**–**f** was performed once. All box plots (**d** and **f**) feature a median (black line), 25th and 75th percentiles (box boundaries), and 5th and 95th percentiles (whiskers). See the Supplementary Data for full statistical breakdown. Source data are provided as a Source Data file.

binder could function at the N- or C-terminus of a CYpHER. The rigid linker in CT-4212-3 is to prevent formation of aberrant cystines between the two CDPs. Both molecules were tested on polyclonal 293T, H1650, and MDA-MB-231 cell populations transduced (via lentivirus) to express PD-L1-GFP. In all three populations, PD-L1 was trafficked from the surface by CYpHER (Fig. 2b), as seen in both microscopy and flow cytometry assays (using a non-competitive PD-L1 antibody [clone 22C3], Fig. 2c–e)[29]. Flow cytometric quantitation of per-cell GFP levels demonstrated substantial and consistent surface PD-L1 removal (Fig. 2f, h, j), as well as overall flow-assessed PD-L1-GFP reduction in all cases (Fig. 2g, i, k). The degree of total PD-L1-GFP reduction varied by cell line and CYpHER. The highest-expressing population, 293T-PDL1-GFP, experienced the largest degree of GFP reduction. This could be caused by better cooperative CYpHER accumulation when more target is present, by saturation of the recycling pathway, or both.

The CYpHER platform is amenable to any target for which surface or soluble elimination would benefit patients beyond simply binding or blocking one site. One such target, with dual roles as both kinase and kinase substrate (as well as other cell-surface-driven functions)[30], is EGFR. It is implicated as a driver of several common and deadly cancers, including glioblastoma, lung cancer, head and neck cancer, and colon cancer[6,31–33]. It is primarily targeted by TKIs or monoclonal

https://doi.org/10.1038/s41467-024-52975-2

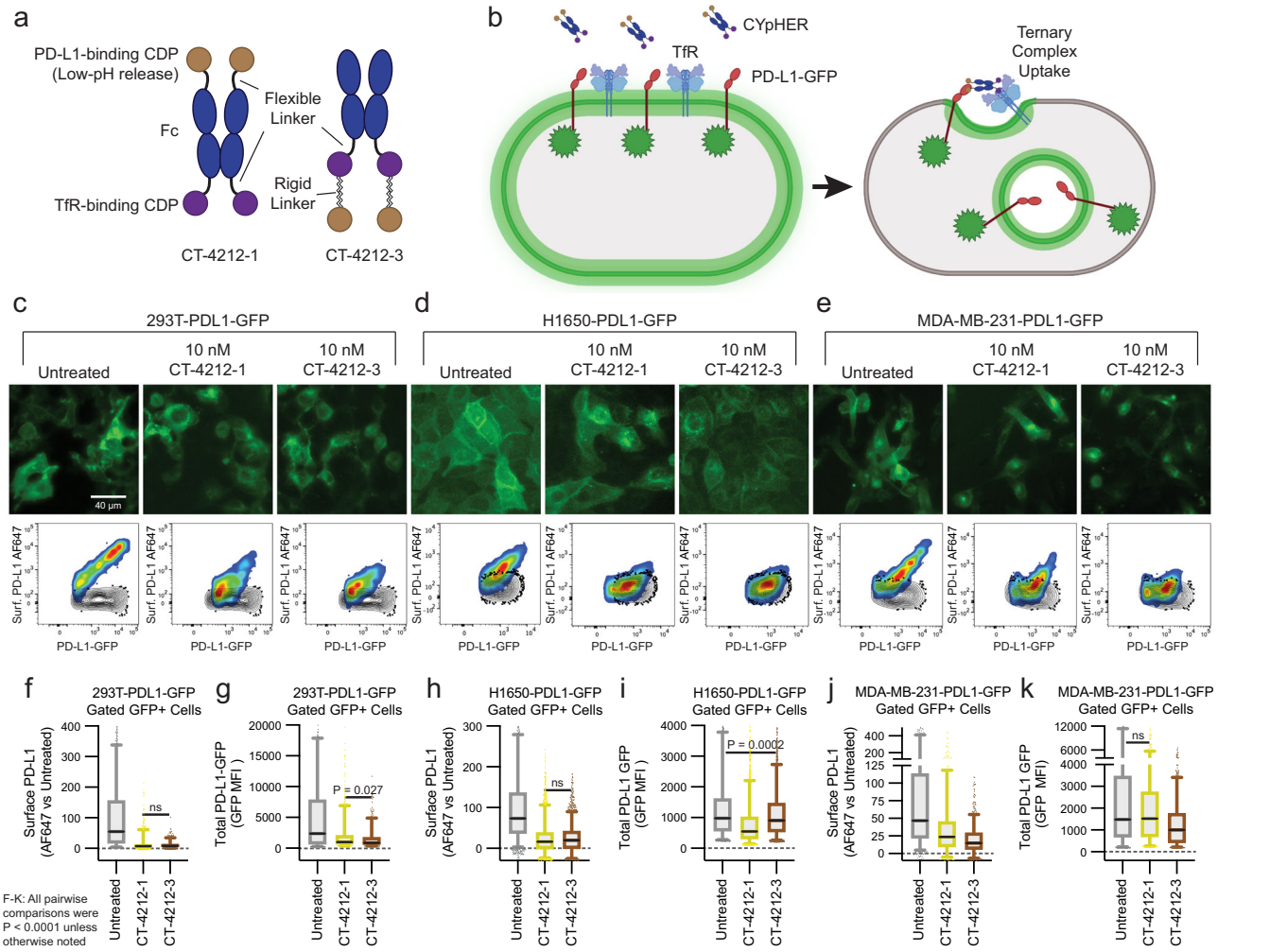

Fig. 2 | PD-L1 CYpHER design and target depletion in cell pools overexpressing PD-L1-GFP. a Two designs of PD-L1 CYpHERs, named CT-4212-1 and CT-4212-3, using a high-affinity TfR-binding CDP and a pH-dependent PD-L1-binding CDP. **b** Illustration of PD-L1-GFP trafficking induced by CYpHER. Pools of 293T cells (**c**), H1650 cells (**d**), and MDA-MB-231 cells (**e**) transduced with lentivirus driving PD-L1-GFP were untreated or incubated with 10 nM CYpHER for 24 h before GFP-channel microscopy (above) and flow cytometry (below) after staining for surface PD-L1. Black contour in flow profiles: cells stained without PD-L1 antibody. Flow cytometry quantitation of normalized surface PD-L1 (**f**, **h**, and **j**) or total PD-L1-GFP (**g**, **i**, and **k**) signal in 293T-PDL1-GFP cells (**f** and **g**), H1650-PDL1-GFP cells (**h** and **i**), and MDA-MB-231-PDL1-GFP cells (**j** and **k**) with or without CYpHER treatment. N cells per sample as follows. **c**, **f**, **g** Untreated, 842; CT-4212-1, 808; CT-4212-3, 598. **d**, **h**, **i** Untreated, 1867; CT-4212-1, 2318; CT-4212-3, 2734. **e**, **j**, **k** Untreated, 823; CT-4212-1, 536; CT-4212-3, 893. For **f**–**k**, within each line and assay, significance by Kruskal–Wallis test with Dunn's correction were all $P < 0.0001$ except: 293T-PDL1-GFP surface PD-L1, CT-4212-1 vs CT-4212-3 ($P = 0.1647$); 293T-PDL1-GFP total GFP, CT-4212-1 vs CT-4212-3 ($P = 0.0027$); H1650-PDL1-GFP surface PD-L1, CT-4212-1 vs CT-4212-3 ($P = 0.0908$); H1650-PDL1-GFP total GFP, Untreated vs CT-4212-3 ($P = 0.0002$); MDA-MB-231-PDL1-GFP total GFP, Untreated vs CT-4212-1 ($P = 0.3139$). Each experiment in **c**–**k** was performed once. All box plots (**f**–**k**) feature a median (black line), 25th and 75th percentiles (box boundaries), and 5th and 95th percentiles (whiskers). See the Supplementary Data for full statistical breakdown. Source data are provided as a Source Data file.

antibodies (mAbs). Patients can benefit for a time, but resistance to these treatments inevitably emerges and remains an area of urgent need for new therapies[34]. These resistance mechanisms are often either a point mutation to reduce TKI activity or an upregulation of another EGFR heterodimerization partner like HER2, HER3, or c-Met. Elimination of EGFR from the surface would drastically reduce EGFR-associated signaling, including kinase-independent signaling[35,36], as it primarily occurs at the plasma membrane.

An EGFR-binding VHH nanobody[37] was engineered into a CYpHER component through similar means to the PD-L1-binding CDP. In one method, a pool of variants with His substitutions was screened in mammalian surface display[28] through four rounds of enrichment; two rounds enriched for high binding at neutral pH (pH 7.4), while the other two enriched for low binding at early endosomal pH (pH 5.5). In the final round of sorting, populations with low (Supplementary Fig. 2A) or high binding at pH 5.5 (Supplementary Fig. 2B) were collected. The primary variant in the pool enriched for low binding in low pH loses roughly half its bound EGFR in tetravalent (streptavidin) stain conditions upon low-pH rinse (Supplementary Fig. 2C), while the dominant variant from the population with high binding at low pH does not have this property (Supplementary Fig. 2D). Fc fusions to each of these molecules, when used as ligands in surface plasmon resonance experiments, verified these properties (Supplementary Fig. 2, E, F); the variant engineered for pH-dependent EGFR release demonstrated higher affinity at neutral pH ($K_D = 16.2 \pm 0.1$ nM at pH 7.4) compared to low pH ($K_D = 61.2 \pm 0.3$ nM at pH 5.8) and the other variant demonstrating slightly lower affinity at neutral pH ($K_D = 10.5 \pm 0.1$ nM at pH 7.4) compared to low pH ($K_D = 7.8 \pm 0.07$ nM at pH 5.8). Both of these represent >10-fold higher affinity vs the reported affinity of the parental nanobody[38]. The pH-dependent release nanobody was named EGFR Nanobody v1.

As an additional allele identification strategy, singleton His scanning (i.e. single His substitutions tested one at a time) was performed on the nanobody in CDRs 1 and 3, as these CDRs are primarily implicated in EGFR-binding[38]. One variant (His Sub 10) was identified in mammalian surface display that lost roughly half its bound EGFR in tetravalent stain conditions upon low-pH rinse (Supplementary Fig. 2G); this was named EGFR Nanobody v2.

Adapting a native ligand for CYpHER

In building the platform, it was apparent that the target-binding domain needn't be an exogenous molecule. As a great many disease-associated target proteins do so by signal transduction mediated by ligand-binding, the ligand presents itself as a natural target-binder that can be adapted, through engineering and affinity/pH maturation, for CYpHER incorporation. In the case of EGFR, EGF itself (a naturally pH-dependent binder which is also a CDP)[39] can be used after engineering it to disable signal transduction capabilities. Rosetta protein modeling software[40,41] was used to design EGF variants that bind to EGFR Domain III in the absence of Domain I, after which studying the EGF:EGFR co-crystal structure (PDB: 1IVO)[42] was used to identify mutations predicted to disrupt Domain I interaction. The end result was a dominant-negative EGF variant a) that binds to Domain III in the absence of Domain I, b) whose Domain I interaction is disrupted to the degree that Domain I impairs binding, and c) that retains the pH-dependent binding of the parent molecule (Supplementary Fig. 3). The details for this design effort are found in the Supplemental Methods. The final variant from this process, EGFd1.5.36, was then used in CYpHER molecules.

EGFR CYpHER induces EGFR surface clearance and elimination

A candidate EGFR CYpHER, CT-1212-1, was produced using a high-affinity TfR-binding CDP and EGFR Nanobody v1 (Fig. 3a–c). The molecule demonstrated good expression and assembly with negligible aggregate after capture from supernatant and buffer exchange. 293T cells expressing a variable level of EGFR-GFP, expected to undergo target internalization upon CYpHER treatment similar to PD-L1-GFP (Fig. 3d), were dosed and analyzed by microscopy and flow cytometry (staining with non-competitive anti-EGFR clone 199.12)[43] for total EGFR-GFP and surface EGFR (Fig. 3e). As a population, cells demonstrated >80% reduction of surface EGFR and ~50% reduction of total EGFR-GFP signal at 24 h, which was validated by Western blot of lysate from flow-sorted, viable cells (Fig. 3f). Viable cells were studied because dead cells and debris are not metabolically active and cannot drive endolysosomal trafficking of targets. The flow profile was not "shifted" en-masse by CYpHER treatment; instead, much of the reduction occurred in those cells with the highest initial EGFR levels. Partitioning flow profiles by surface EGFR supported this observation (Fig. 3g), where the cells with the most surface EGFR experienced the greatest proportional loss. Meanwhile, time-course experiments demonstrated that surface EGFR clearance is rapid (near maximal effect after 1 h), consistent with rapid TfR-mediated uptake, while EGFR-GFP signal loss takes more time, likely due to the slower kinetics of lysosomal degradation vs surface internalization (Fig. 3h, i). This was corroborated by labeling 293T-EGFR-GFP cells with LAMP1-RFP via baculovirus (BacMam 2.0, Invitrogen) for 24 h and then treating cells with DyLight 755-conjugated CT-1212-1 for 0, 1, or 4 h (Fig. 3j). Lysosomal RFP signal overlapped with EGFR-GFP foci more often and more intensely at 4 h than at 1 h. CYpHER signal was also more intense overall at 4 h than at 1 h. The CYpHER signal at 4 h was within several intracellular compartments, including the lysosome, indicating some of the CYpHER being trafficked alongside EGFR-GFP to the lysosome and/or a portion of TfR undergoing normal lysosomal turnover bringing CYpHER with it.

We focus much of our protein trafficking data on surface clearance instead of total protein elimination. First, removal of EGFR from the plasma membrane separates it from access to both ligand and downstream signaling modulators like KRas. Second, after endosomal release, actual elimination vs recycling of protein is highly context-dependent, involving cell-specific recycling kinetics and saturable trafficking modulators[44]. Third, proteins in the process of synthesis can be detected as total protein but can neither signal effectively nor be accessed by CYpHER.

We explored surface EGFR clearance rates on a panel of non-small cell lung cancer (NSCLC) cell lines which include various drug-resistance mechanisms that can occur in patients: H1650 (EGFR with exon 19 deletion and PTEN knockout), H1975 (EGFR with L858R and T790M mutations [the latter rendering it resistant to 1st generation EGFR TKIs] along with activating G118D mutation in PIK3CA), A549 (wild type EGFR with activated KRas G12S), and H358 (wild type EGFR with activated KRas G12C). They represent a range of total surface levels and ratios of EGFR and TfR (the latter measured with non-competitive clone OKT9)[45] (Fig. 4a). All four lines responded to CYpHER for surface EGFR clearance (Fig. 4b), with rapid kinetics (1 h) and to a much greater degree than seen with cetuximab, a molecule known to induce surface clearance and overall protein reduction via induction of ubiquitin-mediated uptake[2,3]. We also confirmed that CYpHER remains detectible on the cell surface 24 h after media exchange, where cetuximab does not (Fig. 4c).

CYpHERs with any of the three engineered EGFR binders clear surface EGFR

The other two engineered EGFR binders were also incorporated into CYpHER molecules (Fig. 4d). The same Fc with a high-affinity TfR-binding CDP (separated by Gly-Ser linker) was the starting point. The nanobodies were fused via a Gly-Ser linker to the N-terminus of the Fc domain as was done in CT-4212-1; the nanobody's N-terminus is at the EGFR Domain III interface[38], so this format is optimal for EGFR binding. As with EGFR Nanobody v1 and CT-1212-1, EGFR Nanobody v2 was incorporated into CT-6212-1. Conversely, the C-terminus of EGF is adjacent to the EGFR Domain III interface[42], so fusion via its N-terminus is optimal; it was incorporated in a similar format to that of CT-4212-3, producing CT-5212-3.

Surface EGFR levels in A549 cells were reduced after 24 h CYpHER treatment with all 3 designs, including after media exchange and growth without drug for another 24 h ("Withdrawal") (Fig. 4e); as EGFR turnover in the absence of ligand is fairly rapid (~6–10 h on most cell lines)[46], this suggested retention of activity via catalytic mechanism. All three CYpHER molecules were still present on the surface after a 24 h drug withdrawal (Fig. 4f).

CT-1212-1 was tested for up to 3 days in the four NSCLC cell lines (A549, H1975, H358, and H1650). All four cancer lines had rapid (within 1 h) reduction of surface EGFR, which was reduced by 55–81% of untreated after 24 h (Fig. 4g and Supplementary Fig. 4); this reduction was maintained for at least 3 days. Additionally, 24 h without drug after 24 h of treatment ("withdrawal") still yielded surface EGFR levels markedly lower than untreated cells; in A549 and H1975 cells, this effect is durable out to 3 days after drug withdrawal, at which point CYpHER is still observed on the cell surface (Supplementary Fig. 5). Different cell lines are expected to have different uptake and rebound kinetics, so this phenomenon is not assumed to be universal. We also evaluated surface TfR levels (Supplementary Fig. 6). In A549 and H1975 cells, mild fluctuations that may represent drug-dependent effects on TfR expression and/or trafficking, but are not persistent with continuous drug exposure, are apparent. In the lines with the highest TfR levels (H358 and H1650), a more substantial and sustained reduction of surface TfR occurred that took 24 h to reach these low levels and largely returned to normal after 24 h of withdrawal. Their higher levels of surface TfR may facilitate CYpHER-induced multimerization, which is known to alter TfR trafficking[47].

https://doi.org/10.1038/s41467-024-52975-2

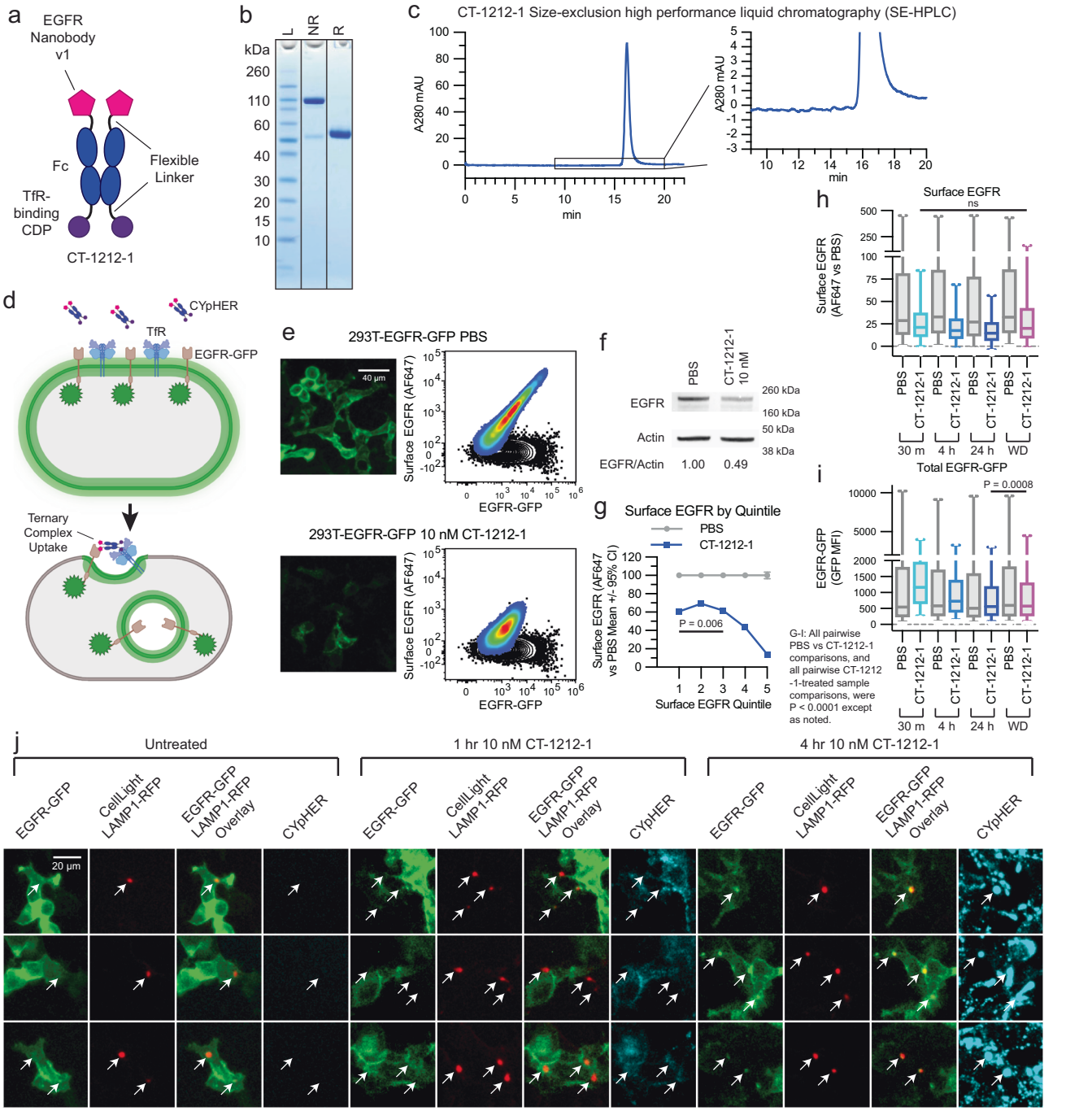

Fig. 3 | EGFR CYpHER based on VHH nanobody. a CT-1212-1 design. **b** CT-1212-1 SDS-PAGE Coomassie stain. NR: non-reduced. R: DTT-reduced. **c** SE-HPLC of CT-1212-1; right is zoomed. **d** EGFR-GFP trafficking by CYpHER in 293T-EGFR-GFP cells. **e** 293T-EGFR-GFP cells treated 24 h with PBS or 10 nM CT-1212-1 before either GFP microscopy (left) or flow cytometry after staining for surface EGFR (right). Black contour: unstained cells. **f** 293T-EGFR-GFP cells treated with PBS or 10 nM CT-1212-1 for 24 h and flow sorted for viable (DAPI-) cells prior to Western blotting. Full blot in Supplementary Fig. 13. **g** Same 293T-EGFR-GFP cells and treatment as **e**, stratified by surface EGFR quintile and showing normalized surface EGFR stain per cell. Two-tailed Kolmogorov–Smirnov test, PBS vs CT-1212-1 pairwise were all $P < 0.0001$, Quintile 1 vs Quintile 3 was $P = 0.0062$, all other CT-1212-1 quintile pairwise comparisons were $P < 0.0001$. **h**, **i** 293T-EGFR-GFP cells dosed with PBS or 10 nM CT-1212-1 for 30 min, 4 h, 24 h, or 24 h followed by 24 h without drug ("Withdrawal") were flow analyzed for surface EGFR (**h**) or total EGFR-GFP (**i**) as in **e**, with EGFR stain (**h**) or total EGFR-GFP (**i**) fluorescence per cell shown. N cells per sample in **h** and **i**: PBS 30 min [m], 14806; 1212-1 30 m, 12117; PBS 4 hour [h], 15289; 1212-1 4 h, 13400; PBS 24 h, 14449; 1212-1 24 h, 12588; PBS Withdrawal [WD], 14487; 1212-1 WD, 13972. For surface EGFR (**h**), PBS vs CT-1212-1 pairwise were all $P < 0.0001$ via two-tailed Kolmogorov–Smirnov [KS] test. CT-1212-1 samples pairwise by Kruskal–Wallis test with Dunn's correction [KWD]: 30 min vs Withdrawal was not significant ($P > 0.9999$), all others $P < 0.0001$. For total EGFR-GFP (**i**), PBS vs CT-1212-1 pairwise were all $P < 0.0001$ via two-tailed KS test. All four CT-1212-1 samples by KWD: 24 h vs Withdrawal was $P = 0.0008$, all others $P < 0.0001$. **j** 293T-EGFR-GFP Cells (24 well dish, 500 µL media per well) were treated with 50 µL CellLight Lysosomes-RFP (delivering gene for LAMP1-RFP) for 24 h, after which they were untreated or treated with 10 nM DyLight 755-labeled CT-1212-1 for 1 or 4 h and then imaged on the GFP, RFP, and near IR channels. Arrows indicate location of LAMP1-RFP foci (i.e., lysosomes). Each experiment in **e**–**j** was performed once (**e**, **g**–**j**) or twice (**f**) producing similar results. All box plots (**h** and **i**) feature a median (black line), 25th and 75th percentiles (box boundaries), and 5th and 95th percentiles (whiskers). See the Supplementary Data for full statistical breakdown. Source data are provided as a Source Data file.

https://doi.org/10.1038/s41467-024-52975-2

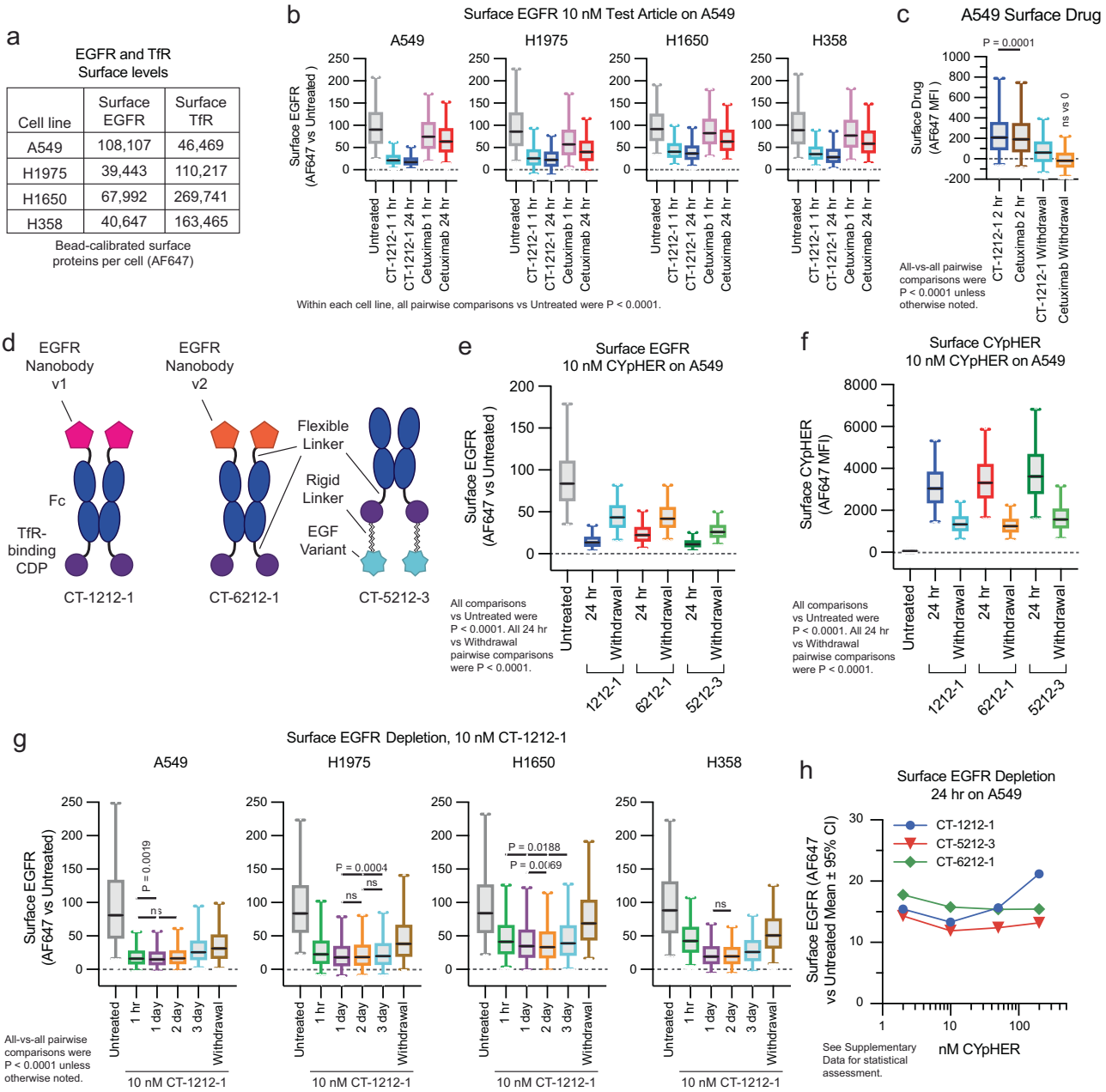

We also tested whether we could observe a hook effect. This phenomenon has been documented for some bispecific TPD molecules, wherein target depletion is blunted if the drug concentration is so high that separate drug molecules occupy each respective partner (preventing ternary complex formation)[48]. At all doses of CT-1212-1, CT-5212-3, and CT-6212-1 evaluated (2–200 nM), surface EGFR levels on A549 cells were reduced compared to untreated cells after 24 h of treatment (Fig. 4h). The degree of EGFR reduction by CT-1212-1 was modestly blunted at 200 nM compared to lower doses, whereas CT-5212-3 and CT-6212-1 show minimal variation over this concentration range. This suggests that the effect, if any, is mild and the nature of the molecule (binder and/or modular organization) may have some impact. Effects may also differ by cell line, target, and metabolic state.

CYpHER-driven EGFR intracellular sequestration

We evaluated EGFR trafficking in a knock-in A549-EGFR-GFP cell line using CT-1212-1 and variants thereof (Fig. 5a) that used heterodimeric Fc domains to alter EGFR- and TfR-binding valence. All four molecules that contained at least one EGFR-binder and at least one TfR-binder drove EGFR-GFP from the membrane into intracellular compartments (Fig. 5b), with flow assays demonstrating this effect to be dose-dependent in 3 of 4 drugs and mostly retained by all after 24 h drug withdrawal (Fig. 5c). Control molecules containing a non-EGFR-binding nanobody or a non-TfR-binding CDP did not induce trafficking (Fig. 5d); this trafficking is not associated with a reduction in total EGFR-GFP in this line (Supplementary Fig. 7). We confirmed the rapid activity of the mechanism, showing this internalization phenotype after only 20 min of treatment (Fig. 5e). We also tested holoTF competition, as our TfR-binding CDP binds to the same site on TfR as transferrin[25]. Both EGFR-GFP internalization (Fig. 5f) and surface EGFR clearance (Fig. 5g) were retained in the presence of human holoTF, with only mild suppression of activity at 1000x molar levels of holoTF versus CYpHER.

CYpHER catalytic target uptake

Our experiments with drug withdrawal strongly suggest a catalytic mechanism of action where one drug molecule can induce uptake of multiple target molecules, as we see both retention of activity and

https://doi.org/10.1038/s41467-024-52975-2

Fig. 4 | Performance comparison of different EGFR CYpHER designs. a A549, H1975, H1650, and H358 cells were flow analyzed alongside calibration beads to quantitate surface EGFR and TfR protein levels. **b** Normalized surface EGFR levels in the four lines after 1 or 24 h treatment with 10 nM CT-1212-1 or cetuximab, showing surface EGFR stain per cell by flow. N cells per sample as follows. A549: Untreated, 17129; CT-1212-1 1 h, 17641; CT-1212-1 24 h, 19326; Cetuximab 1 h, 16815; Cetuximab 24 h, 18083. H1975: Untreated, 5544; CT-1212-1 1 h, 6091; CT-1212-1 24 h, 6593; Cetuximab 1 h, 4847; Cetuximab 24 h, 5400. H1650: Untreated, 4789; CT-1212-1 1 h, 5258; CT-1212-1 24 h, 5460; Cetuximab 1 h, 5548; Cetuximab 24 h, 5541. H358: Untreated, 7846; CT-1212-1 1 h, 8239; CT-1212-1 24 h, 7834; Cetuximab 1 h, 8120; Cetuximab 24 h, 8409. Within each of the four cell lines (A549, H1975, H1650, H358), all five samples were compared to one another by Kruskal–Wallis test with Dunn's correction [KWD]; all comparisons for all cell lines were $P < 0.0001$. **c** A549 cells incubated with 10 nM CT-1212-1 or cetuximab for 2 h or for 2 h followed by 24 h without drug ("Withdrawal") followed by staining for human IgG to quantitate surface drug levels, showing surface IgG stain per cell by flow. N cells per sample: CT-1212-1 2 h, 6336; Cetuximab 2 h, 6126; CT-1212-1 Withdrawal [WD], 7335; Cetuximab WD, 7187. All vs all by KWD; CT-1212-1 2 h vs Cetuximab 2 h was $P = 0.0001$, all others $P < 0.0001$. Furthermore, all samples were compared via one sample two-tailed T test to 0; Cetuximab Withdrawal was $P = 0.37$, all others $P < 0.0001$. **d** EGFR CYpHER designs. **e** Surface EGFR levels in A549 cells incubated with 10 nM CYpHER for 24 h or for 24 h followed by 24 h without CYpHER ("Withdrawal"), showing surface EGFR stain per cell by flow. N cells per sample – see Source Data for details. All treated samples vs Untreated by KWD were $P < 0.0001$. All 24 h vs Withdrawal samples compared by Kolmogorov–Smirnov [KS] test were $P < 0.0001$. **f** Same treatment as **e** but staining for human Fc to quantitate surface CYpHER levels, showing surface Fc stain per cell by flow. N cells per sample – see Source Data for details. All treated samples vs Untreated by KWD were $P < 0.0001$. All 24 h vs Withdrawal samples compared by Kolmogorov–Smirnov [KS] test were $P < 0.0001$. **g** A549, H1975, H1650, and H358 cells untreated or treated with 10 nM CT-1212-1 for 1 h, 1 day, 2 days, 3 days, or 1 day followed by 1 day without drug ("Withdrawal") then analyzed by flow cytometry to see surface EGFR levels per cell. N cells per sample – see Source Data for details. All samples vs all within a cell line by KWD: A549, 1 h vs 1 day $P = 0.0019$, 1 h vs 2 day $P = 0.9911$, all others $P < 0.0001$; H1975, 1 day vs 2 day $P = 0.8709$, 1 day vs 3 day $P = 0.0004$, 2 day vs 3 day $P = 0.3246$, all others $P < 0.0001$; H1650, 1 h vs 3 day $P = 0.0188$, 1 day vs 2 day, $P = 0.0069$, all others $P < 0.0001$; H358, 1 day vs 2 day $P > 0.9999$, all others $P < 0.0001$. **h** A549 cells treated for 24 hr with 2 nM, 10 nM, 50 nM, or 200 nM CYpHER then analyzed by flow cytometry for surface EGFR levels to show surface EGFR levels per cell by flow. N cells per sample – see Source Data for details. Experiments in **b**, **c**, **e**, and **f** were performed once. All box plots (**b**, **c**, **e**–**g**) feature a median (black line), 25th and 75th percentiles (box boundaries), and 5th and 95th percentiles (whiskers). See the Supplementary Data for full statistical breakdown. Source data are provided as a Source Data file.

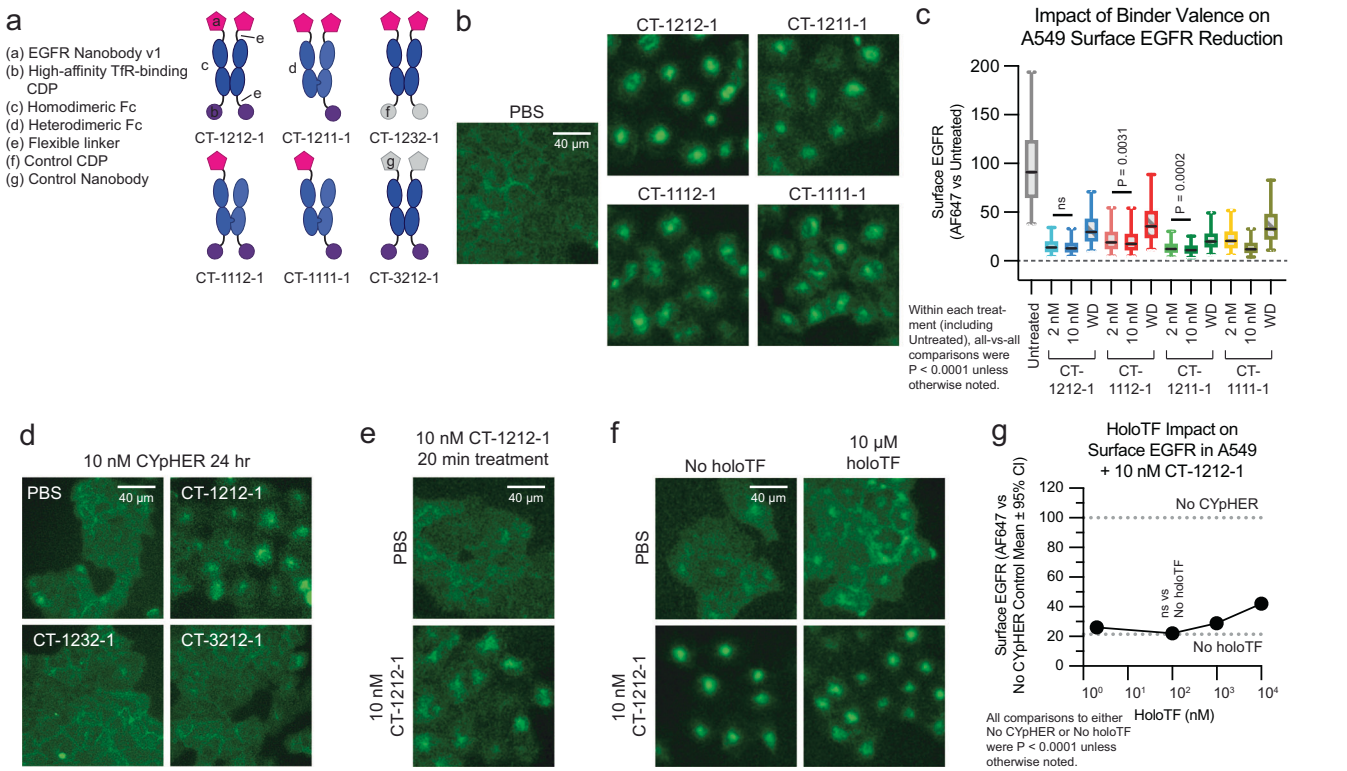

Fig. 5 | EGFR trafficking upon CYpHER treatment. a Designs of various EGFR CYpHERs and control molecules. **b** A549-EGFR-GFP (knockin) cells treated with PBS or 10 nM CYpHER for 48 h with drug and imaged for GFP localization. **c** A549 cells treated with 2 or 10 nM CYpHER for 24 hrs, or 10 nM CYpHER for 24 h followed by 24 h drug withdrawal, and assayed by flow cytometry for surface EGFR per cell. N cells per sample as follows: Untreated, 3598. CT-1212-1: 2 nM, 2979; 10 nM, 3288; Withdrawal [WD], 2795. CT-1112-1: 2 nM, 3527; 10 nM, 3286; WD, 3135. CT-1211-1: 2 nM, 2339; 10 nM, 3018; WD, 2250. CT-1111-1: 2 nM, 3412; 10 nM, 3532; WD, 2516. All-vs-all within treatments (including Untreated) by Kruskal–Wallis [KW] test: CT-1212-1, 2 nM vs 10 nM $P = 0.1494$, all others $P < 0.0001$; CT-1112-1, 2 vs 10 nM $P = 0.0031$, all others $P < 0.0001$; CT-1211-1; 2 vs 10 nM $P = 0.0002$, all others $P < 0.0001$; CT-1111-1, all $P < 0.0001$. **d** A549-EGFR-GFP cells imaged for GFP localization after 24 h treatment with 10 nM CYpHER (CT-1212-1) or control molecule (CT-1232-1 or CT-3212-1). **e** A549-EGFR-GFP cells imaged for GFP localization after 20 min treatment with PBS or 10 nM CT-1212-1. **f** A549-EGFR-GFP cells treated without or with 10 µM human holoTF for 15 min followed by addition of PBS or 10 nM CT-1212-1 for 4 h and imaged for GFP localization. **g** Same experimental design as in **f** except altered amount of holoTF and analyzed by flow cytometry for surface EGFR. Dashed lines indicate quantitation of surface EGFR in untreated cells (upper) or cells treated with 10 nM CT-1212-1 but no holoTF (lower). Each treatment vs No CYpHER (100% line) by Kruskal–Wallis test with Dunn's correction [KWD] was $P < 0.0001$. Each CYpHER + holoTF treatment vs CYpHER + no holoTF ("No holoTF" line at ~21%) by KWD: 100 nM holoTF $P = 0.9831$, all others $P < 0.0001$. Experiments in **b**–**g** were performed once (**c**, **f**, **g**) or twice (**b**, **d**, **e**) with similar results. All box plots (**c**) feature a median (black line), 25th and 75th percentiles (box boundaries), and 5th and 95th percentiles (whiskers). See the Supplementary Data for full statistical breakdown. Source data are provided as a Source Data file.

https://doi.org/10.1038/s41467-024-52975-2

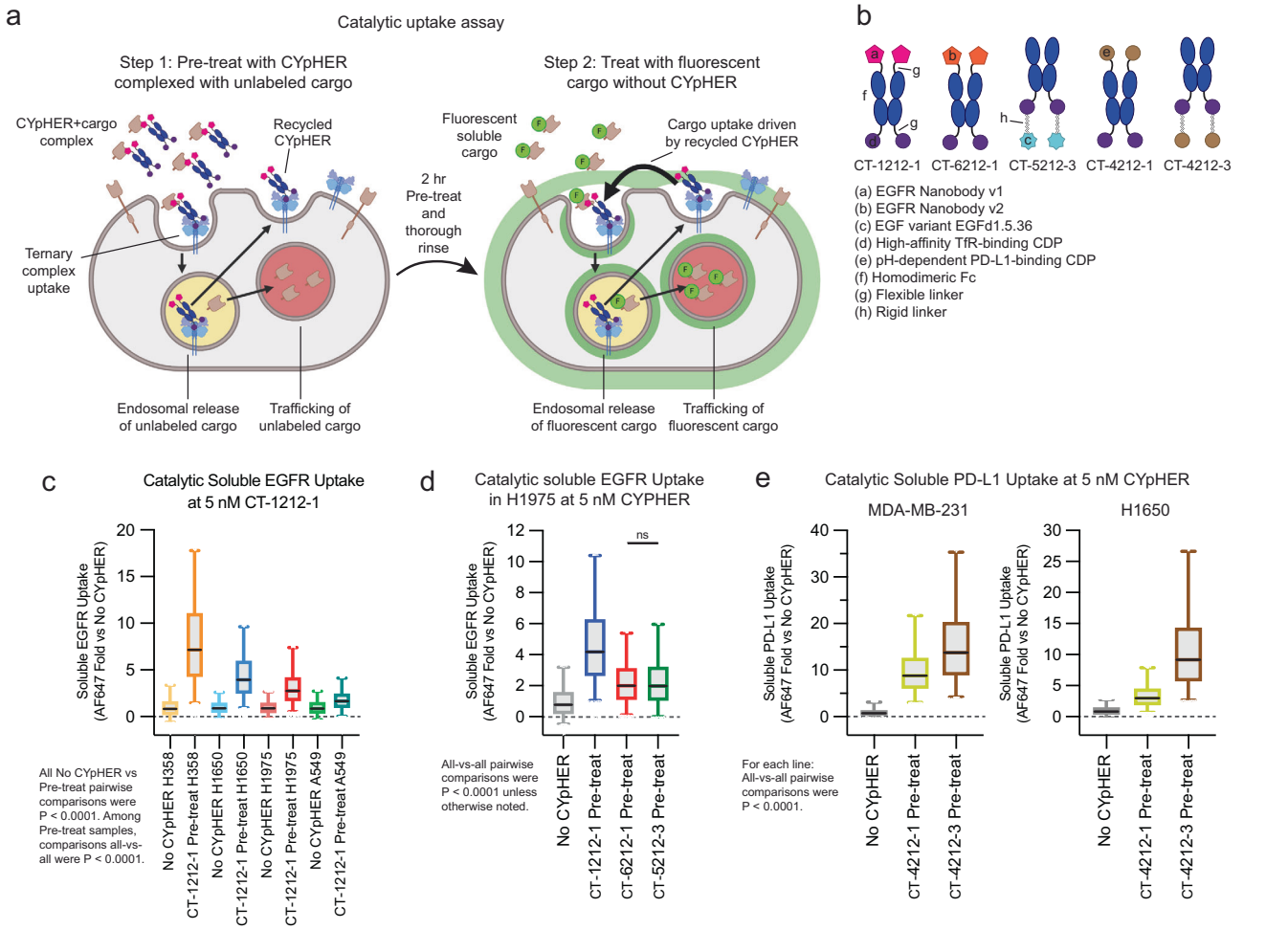

Fig. 6 | Catalytic soluble cargo uptake by CYpHER. a Experimental design to quantitate fluorescent soluble cargo uptake in cells pre-treated with cargo-saturated CYpHER. Step 1: CYpHER is saturated with target (2:1 target:binding moiety ratio), then applied to cells for 2 h. Step 2: After cells are thoroughly rinsed, new fluorescently-labeled soluble target is added to cells. Fluorescence accumulation is increased by CYpHER pre-treatment. **b** Designs and elements of CYpHERs used. **c** Soluble EGFRvIII uptake per cell after 24 h incubation with A549, H1650, H1975, or H358 cells either untreated (to quantitate passive uptake) or pre-treated for 2 h with unlabeled-EGFR-saturated 10 nM CT-1212-1, normalized to each cell line's untreated uptake levels. N cells per sample as follows. H358: No CYpHER, 6309; CT-1212-1 Pre-treat, 5901. H1650: No CYpHER, 6622; CT-1212-1 Pre-treat, 6567. H1975: No CYpHER, 6087; CT-1212-1 Pre-treat, 5858. A549: No CYpHER, 7584; CT-1212-1 Pre-treat, 7848. Each line (H358, H1650, H1975, A549), pre-treatment vs Untreated via two-tailed Kolmogorov–Smirnov [KS] test were $P < 0.0001$. Pre-treatments all-vs-all by Kruskal–Wallis test with Dunn's correction [KWD] were $P < 0.0001$. **d** Soluble EGFRvIII uptake per cell in H1975 cells as in **c** comparing CT-1212-1, CT-6212-1, and CT-5212-3. N cells per sample: CT-1212-1 Pre-treat, 5778; CT-6212-1 Pre-treat, 5277; CT-5212-3 Pre-treat, 5540. All-vs-all by KWD: CT-6212-1 Pre-treat vs CT-5212-3 Pre-treat $P > 0.9999$, all others $P < 0.0001$. **e** Soluble PD-L1 uptake per cell as in **c** except with soluble PD-L1 as cargo, comparing CT-4212-1 and CT-4212-3 in MDA-MB-231 (left) or H1650 (right) cells. N cells per sample as follows. MDA-MB-231: No CYpHER, 22023; CT-4212-1 Pre-treat, 6667; CT-4212-3 Pre-treat, 7398. H1650: No CYpHER, 20807; CT-4212-1 Pre-treat, 7546; CT-4212-3 Pre-treat, 7215. Within each cell line, all-vs-all KWD were $P < 0.0001$. Each experiment in **c**–**e** was performed once. All box plots (**c**–**e**) feature a median (black line), 25th and 75th percentiles (box boundaries), and 5th and 95th percentiles (whiskers). See the Supplementary Data for full statistical breakdown. Source data are provided as a Source Data file.

retention of CYpHER molecules on the surface of cells after 24 h drug withdrawal. We developed an assay to further evaluate catalytic uptake of soluble cargo (Fig. 6a and Supplementary Fig. 8). We first demonstrated that cells specifically take up soluble target:CYpHER complexes. Cells were exposed to CYpHER saturated with fluorescently labeled target for 2 h, permitting time for target uptake and for CYpHER (via TfR) to cycle in and out of the cell several times. This yielded specific target uptake (Supplementary Fig. 8, bars 1 vs 2 [2 h] and bars 3 vs 5 [24 h]). Next, the assay was modified to look for uptake of newly introduced target after the initial 2 h uptake followed by removal of all soluble CYpHER from the system. In step 1 of this assay, cells are exposed to CYpHER saturated with unlabeled target for 2 hrs. Then the cells are thoroughly rinsed to remove all soluble molecules and then exposed to fluorescent soluble target alone for 24 h. Any fluorescent target uptake during these 24 h, in excess of that seen by cells that were not pre-exposed to CYpHER, is due to the catalytic activity of CYpHER molecules that have already cycled and released their non-fluorescent cargo (Supplementary Fig. 8, bars 3 vs 4). With this assay, using various CYpHER designs (Fig. 6b), we saw catalytic CYpHER-driven uptake of cargo with all CYpHER molecules and cell lines tested. Fluorescent soluble EGFRvIII uptake via CT-1212-1 in A549, H1650, H1975, and H358 cell lines (Fig. 6c), was seen, with catalytic uptake (normalized to passive uptake without CYpHER, which is likely via pinocytosis) at levels that vary by cell line. The degree of catalytic uptake also changed dependent on the nature of the target-binder (Fig. 6d). Additionally, as demonstrated using PD-L1 CYpHERs and

https://doi.org/10.1038/s41467-024-52975-2

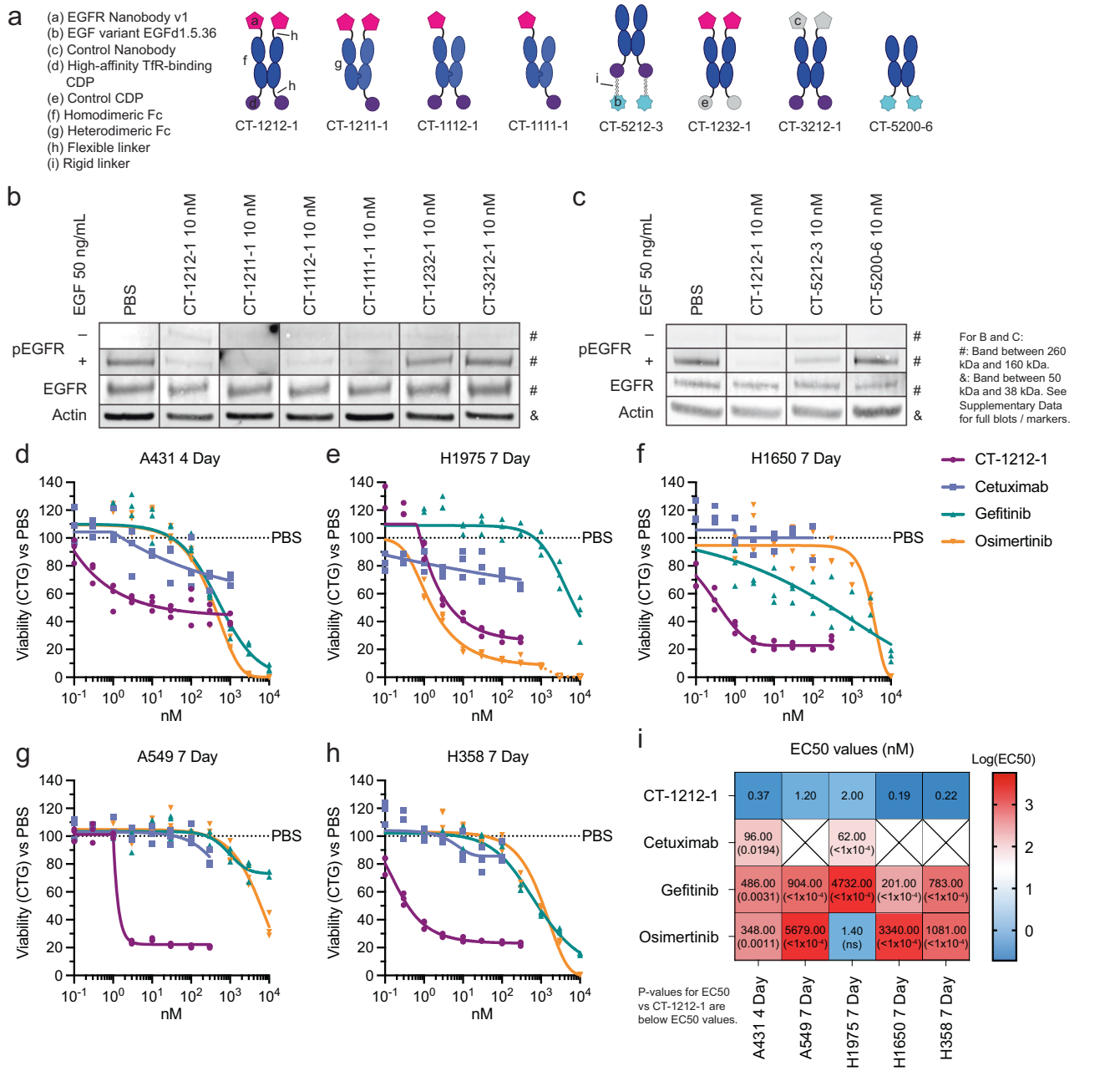

Fig. 7 | Pharmacodynamic effects of CYpHER. a Designs of various EGFR CYpHERs and control molecules. **b** and **c** A549 cells (unsorted, thus including live and dead cells) treated for 24 h with PBS, 10 nM CYpHER, or 10 nM control molecule followed by no treatment ("−", EGFR, Actin) or addition of 50 ng/mL EGF for 30 min ("+") and analyzed by Western blot for pY1068 EGFR ("−" and "+"), total EGFR, or actin. Full blots in Supplementary Figs. 14 and 15. **d**–**h** 96 well plate growth for 4 days (A431) or 7 days (all others) with single dose (no media exchange) of CT-1212-1, cetuximab, gefitinib, or osimertinib in A431 (**d**), H1975 (**e**), H1650 (**f**), A549 (**g**), and H358 (**h**) cells. After treatment, cell levels per well were quantitated by CellTiter-Glo 2.0 [CTG] assay. $N = 3$ wells per condition. See panel **i** for EC50 values and P values vs CT-1212-1; see Supplementary Data for details on statistical analysis. **i** EC50 values of the experiments in **d**–**h** from asymmetric sigmoidal (5PL) curve fit. Empty "X" box indicates no effect, as defined by failure to suppress growth by 20% at any dose tested. Experiments in **b**–**h** were conducted once (**b**, **c**, **h**) or twice (**d**–**g**) with similar results. See the Supplementary Data for full statistical breakdown. Source data are provided as a Source Data file.

soluble PD-L1, the format of the CYpHER (Fig. 6e) had an impact. In all cases, uptake of soluble target in excess of passive uptake was seen, demonstrating a catalytic mechanism of action for CYpHER.

Pharmacodynamic effects of CYpHER in vitro

Having established target depletion, we tested how CYpHER alters EGFR-mediated signaling and cell growth (Fig. 7). Using various CYpHER and control molecules (Fig. 7a), we investigated ligand-induced signaling, where both surface clearance and competitive binding to EGFR could have impacts. Stimulating CYpHER-treated cells with EGF produced no increased EGFR phosphorylation in CT-1212-1-treated cells (Fig. 7b), suggesting any remaining EGFR on the surface is blocked by the drug or is otherwise signaling-incapable. The valence-altering variants (CT-1211-1, CT-1112-1, CT-1111-1) had the same effect, but control molecules CT-1232-1 (non-TfR-binding CDP) and CT-3212-1 (non-EGFR-binding nanobody) did not, demonstrating that both TfR- and EGFR-binding functions are necessary together to block ligand-induced activation of EGFR. CYpHER containing the EGF variant was also tested (Fig. 7c); in contrast to the nanobody-containing CYpHER series, CT-5212-3-treated cells showed some residual EGFR

phosphorylation in response to EGF, suggesting the EGF variant on the CYpHER provides less complete blockade of the EGF-binding site of the residual surface-resident EGFR. Further affinity maturation of the variant may improve its ability to competitively inhibit EGF stimulation under these conditions. Meanwhile, the EGF variant itself (in the form of Fc fusion CT-5200-6) did not induce EGFR phosphorylation, confirming its capacity as a dominant-negative EGF.

As head and neck cancer (e.g., HNSCC) and lung cancer (e.g., NSCLC) are commonly treated with EGFR-targeting agents[6,33], CT-1212-1 was tested for growth suppression in several relevant cell lines: head and neck cancer line A431 (with a massive duplication of the EGFR gene), and the four NSCLC lines H1650, H1975, A549, and H358. All of these lines were tested alongside clinical EGFR-targeted drugs cetuximab (EGFR mAb), gefitinib (1st generation EGFR TKI), and osimertinib (3rd generation EGFR TKI) (Fig. 7d–i). CT-1212-1 suppressed growth across all cancer types and mutational profiles tested. Moreover, It had higher potency than the three clinical comparators in all five lines, with the exception of comparable potency with osimertinib in H1975 cells containing the T790M mutation against which osimertinib was originally developed[49].

The potency of CYpHER in KRas mutant lines A549 (G12S) and H358 (G12C) led us to ask to what degree EGFR signaling and/or iron uptake disruption is contributing to the cell growth inhibition (Supplementary Fig. 9). Reducing TfR-binding valence or affinity modestly reduced potency. Using ferric ammonium citrate (FAC), a cell-penetrant chelated iron supplement, FAC prevented the CT-1212-1 growth disruption on A549 cells. Despite expressing mutant KRas G12S, A549 cells still respond to 1 ng/mL EGF (an amount consistent with tumor parenchyma levels[50]) in the media by demonstrating a migratory phenotype alongside increased growth, both of which were completely or partially (respectively) suppressed by CT-1212-1 but not CT-3212-1 (control that binds TfR but not EGFR) when FAC is present. Additionally, we tested a colon cancer cell line with wild type KRas and high, but not constitutively-active, EGFR expression[51,52], since such colon cancers are commonly treated with EGFR-targeting biologics[53]. It demonstrates growth disruption in response to CT-1212-1 but not cetuximab, similar to the NSCLC lines, but its growth is still partially disrupted when FAC is present. These experiments provide additional context to CYpHER growth disruption, in that cells in vitro can be highly sensitive to iron uptake disruption, but CYpHER can still disrupt EGFR-based growth and migration.

As many EGFR-targeted therapeutics (mAbs and TKIs) demonstrate skin toxicities due to the sensitivity of keratinocytes to EGFR suppression[7,54], CT-1212-1 was also tested in primary human dermal keratinocytes (Supplementary Fig. 10). Examining TfR and EGFR on these cells, TfR levels were much lower on these normal cells than on the cancer lines we tested, while EGFR levels are high (Supplementary Fig. 10A). Surface EGFR clearance was observed with CT-1212-1, but with much slower kinetics than seen in the cancer lines (likely due to much lower surface TfR), and no reduction in surface TfR was seen (Supplementary Fig. 10B). In primary keratinocyte growth inhibition assays (Supplementary Fig. 10C), CT-1212-1 demonstrated similar properties to cetuximab, while the TKIs had similar profiles as their activity on the cancer cell lines. Comparative potencies on cancer and keratinocytes suggest CYpHER could have advantages in sparing keratinocytes from growth disruption while still impairing cancer cell growth (Supplementary Fig. 10D).

In light of CYpHER's interactions with TfR and because some TfR-targeting biologics have impacted reticulocyte levels[55,56], we chronically dosed female athymic nude mice with CT-1222-1 for 4 weeks, twice weekly, at doses from 15 µg to 1000 µg. Looking at red blood cells, reticulocytes, total white blood cells, neutrophils, and lymphocytes 48 h after the final dose, blood cell counts were not significantly altered (Supplementary Fig. 11). The mice also did not demonstrate any body weight loss, gross physical responses, or drug-related behavioral changes. Thus, there were no signs that chronic CYpHER exposure in vivo yielded gross toxicity or hematopoietic side effects, in spite of any impact by CYpHER on TfR levels or iron homeostasis in cancer lines in vitro.

In vivo CYpHER pharmacokinetics and pharmacodynamics

To investigate the in vivo pharmacokinetic (PK) properties of the CYpHER candidates, we dosed NCr nu/nu mice with 1.5 mg/kg CT-1212-1, CT-1222-1, CT-1211-1, and CT-1232-1 (Fig. 8a). The nanobody does not cross-react with murine EGFR, so only the murine cross-reactive TfR-binding CDP and the Fc domain would be expected to influence PK. CT-1212-1 has two high-affinity TfR-binding CDPs, CT-1222-1 has two medium-affinity TfR-binding CDPs, CT-1211-1 has one high-affinity TfR-binding CDP, and CT-1232-1 has no TfR-binding capability (Fig. 8a). As measured by ELISA (Fig. 8b), serum levels of the CYpHER molecules demonstrated serum half-lives between 41 and 88 hrs at this dose, with the longest belonging to the non-TfR-binding molecule CT-1232-1. It is likely that TfR binding increases clearance, a phenomenon seen in other studies[55,57], even with the Fc otherwise extending serum residence. Considering that CYpHERs exhibited potency on cancer cells at concentrations as low as 0.2 nM and EGFR surface clearance at concentrations as high as 200 nM, the PK data indicates that serum levels in a therapeutic range may be readily attained with infrequent dosing. The biodistribution to the target tissue (e.g., tumor), as well as the durability of activity given catalytic target clearance in cells even when CYpHER is removed from extracellular fluid, are still to be investigated.

We next tested mice implanted with flank H1975 xenografts and treated for 8 days with CYpHER for any observed pharmacodynamic (PD) effects (Fig. 8c). Female athymic nude mice were implanted with 5×10^6 H1975 cells. After 21 days of growth, mice received three doses of CYpHER on days 0 (enrollment day), 3, and 7. CYpHERs and doses administered were: CT-1212-1 450 µg/dose; CT-1212-1 150 µg/dose; CT-1212-1 30 µg/dose; CT-1222-1 150 µg/dose; and CT-5212-3 150 µg/dose. On day 8, tumors were harvested for Western blotting and histology. Western blotting (Fig. 8d, e) demonstrated a reduction ($P = 0.04$, as normalized to actin) in total EGFR by CT-1222-1 150 µg/dose, and a trend towards EGFR reduction ($P = 0.11$) by CT-1212-1 450 µg/dose; pY1068 blotting was not significantly different between the groups (Supplementary Fig. 12). Histology for EGFR and Ki67 (Fig. 8f, g) demonstrated two phenomena. First, most fields from the CT-1212-1 450 µg/dose and CT-1222-1 150 µg/dose tumors demonstrated altered localization of EGFR (Fig. 8f), visible as marked reduction of membrane EGFR (DAB stain) relative to intracellular levels. Second, automated Ki67 quantitation (Fig. 8g) demonstrated that 8 days of treatment caused a reduction in the proliferation marker Ki67 (percent Ki67 positivity) in the CT-1212-1 450 µg/dose ($P = 0.003$), CT-1212-1 150 µg/dose ($P = 0.0004$), and CT-1222-1 150 µg/dose ($P = 0.0002$) groups vs vehicle. We will note that the ineffectiveness of CT-5212-3 at reducing proliferation suggests that bivalent high-affinity TfR-binding is not sufficient for disrupting H1975 flank tumor growth. As the nanobody-based CYpHERs that reduced proliferation also were more effective at reducing EGF-mediated EGFR phosphorylation than CT-5212-3 (Fig. 7b, c), the EGFR-inhibition capabilities of CYpHER may be driving the effect in vivo. However, CT-5212-3, which has a murine cross-reactive EGFR binder, may also have altered biodistribution dynamics, which could impact tumor accumulation. These, and other variables, are of interest for future studies.

Discussion

Catalytic TPD via CYpHER is a promising approach to durably depleting disease-driving proteins, capable of altering target trafficking and cell behavior both in vitro and in vivo. CYpHER leverages TfR, a protein whose rapid recycling kinetics provide activity across many tumor and cell types. Furthermore, TfR is overexpressed and required for cancer

https://doi.org/10.1038/s41467-024-52975-2

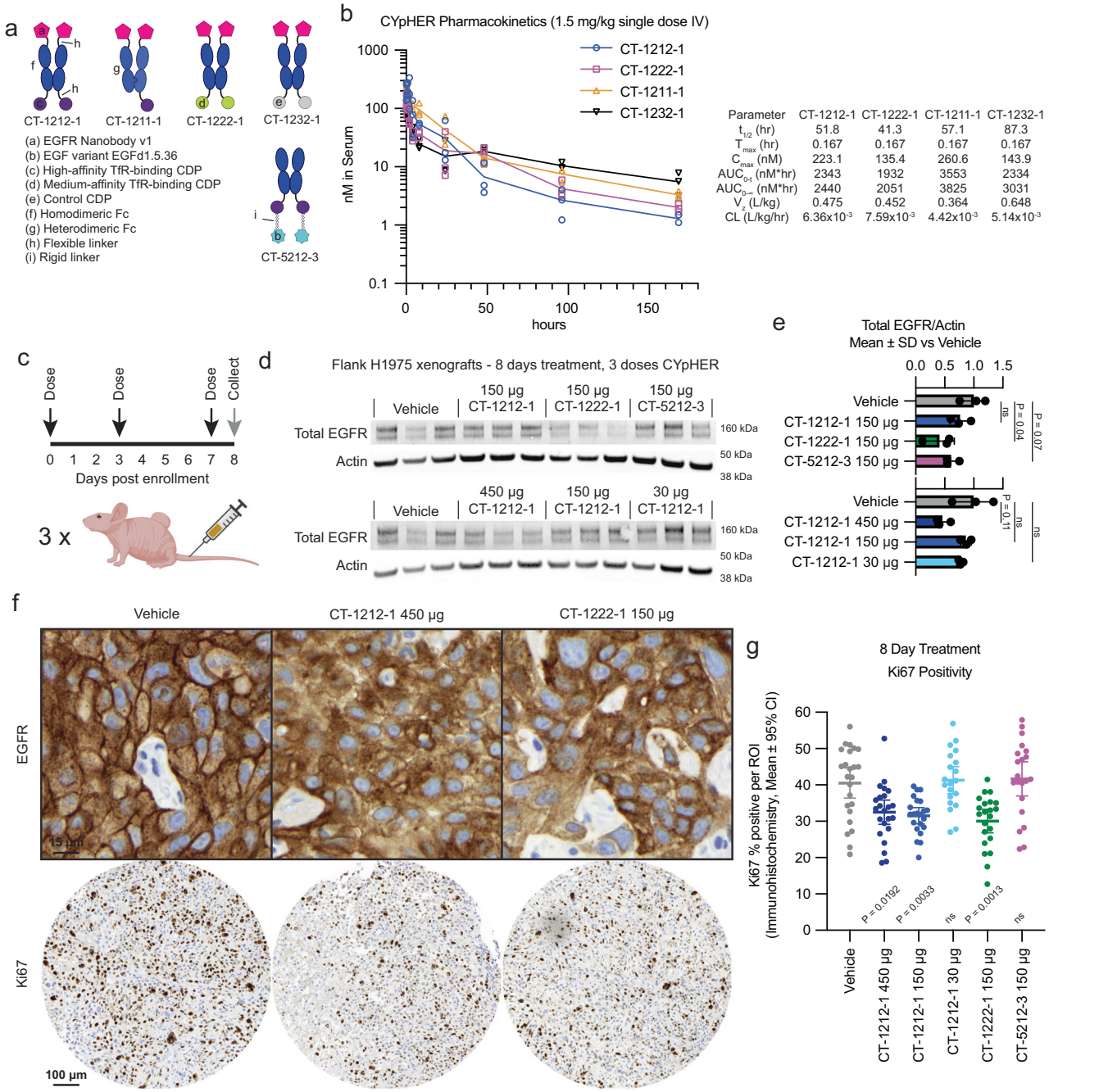

Fig. 8 | Pharmacokinetics and pharmacodynamics of CYpHER in mice. a Designs of CYpHER and control molecules. **b** NCr nu/nu mice were dosed with 1.5 mg/kg CT-1212-1, CT-1211-1, CT-1222-1, or CT-1232-1 IV. Serum was taken after 10 min, 30 min, 1 h, 2 h, 4 h, 8 h, 24 h, 48 h, 96 h, or 168 h. Three mice per time point were analyzed. Samples were quantitated by ELISA for human Fc domain in technical triplicate. $N = 3$ mice per time point. Molecules exhibited a normal biphasic distribution curve, and as such, PK parameters were determined by non-compartmental analysis for IV bolus dosing using PKSolver 2.0. **c** Experimental design for tumor implantation and dosing. Female athymic nude mice (Foxn1^{nu}) were implanted (subcutaneous flank) with 5 ×10^6 H1975 cells. After 21 days, mice were enrolled and dosed IV on days 0 (enrollment day), 3, and 7. On day 8, tumors from three mice per dosage group were harvested and split for Westerns or for histology. **d** Western blot of total EGFR and actin. $N = 3$ mice per condition, all seen in blot. Full blots in Supplementary Fig. 16. **e** Quantitation of the blots from **d**. **f** IHC (hematoxylin/DAB) for total EGFR (top) and Ki67 (bottom) in vehicle, CT-1212-1 450 µg, and CT-1222-1 150 µg groups. Full EGFR fields can be found in Supplementary Fig. 17. **g** Quantitation of Ki67 positivity, derived from 6-9 regions of interest (ROI) per tumor, three tumors per group, pooled for analysis N (ROI) per sample: Vehicle, 24; CT-1212-1 450 µg, 23; CT-1212-1 150 µg, 22; CT-1212-1 50 µg, 20; CT-1222-1 150 µg, 22; CT-5212-1 150 µg, 21. Two-tailed Welch's T test vs Vehicle: CT-1212-1 450 µg, $P = 0.0192$; CT-1212-1, 150 µg, $P = 0.0033$; CT-1222-1 150 µg, $P = 0.0013$; CT-1212-1 50 µg and CT-5212-3 150 µg, $P > 0.9999$. See the Supplementary Data for full statistical breakdown. Each experiment was performed once. Source data are provided as a Source Data file.

cell growth, increasing potential tumor accumulation and reducing the risk of acquired drug resistance. TfR also delivers cargo across the blood-brain barrier, adding CNS proteins as potential targets. Through engineering the target-binding end for pH-dependent release, CYpHER is not reliant on other enzymes for function, and its catalytic activity permits one drug molecule to clear multiple target molecules with more durable function. Lastly, the drug molecules are proteins produced by standard recombinant expression, requiring no chemical modifications and using binder modalities found in other clinically-approved molecules.

CYpHER is a promising approach for cancers driven by RTKs, exemplified by the inexorable challenge of EGFR-driven cancer. Our pilot studies demonstrate a pharmacodynamic effect in tumors, but more studies are necessary to establish potential efficacy in tumor growth inhibition. Meanwhile, the CYpHER platform can approach numerous difficult targets in oncology and CNS disease. The ErbB family of RTKs (e.g., EGFR, HER2, HER3) are all associated with driving cancer and/or inflammation in various tissues and settings, alongside other growth factor and cytokine receptors (e.g., c-Met, FGF receptors, IGF-1 receptors, interleukin receptors). Similar to EGFR, all feature multiple functions like homodimerization, heteroassociation, kinase function, and/or scaffolding for signal transduction. Protein elimination is the only way to completely neutralize all possible disease-causing functions. For CNS conditions, access to the CNS via TfR-mediated transcytosis offers exciting possibilities such as clearing neurodegeneration-associated misfolded proteins (e.g., amyloid, tau, huntingtin) or their inflammatory mediators. CNS metastasis is also a common cause for cancer progression, and TfR-mediated CNS access may prevent this mechanism of recurrence.

In conclusion, CYpHER adds a powerful entry to the TPD field. With catalytic functionality, broad target applicability, good assembly and production, potent and durable alteration of target trafficking, and demonstrable in vivo activity, proteins for which traditional targeted therapeutics have struggled may be approachable, with promising implications to our most insidious and intransigent diseases.

Methods

Study design

This work describes the conception, engineering, and applications of CYpHER, a catalytic targeted protein degradation technology using a recycling receptor (here, TfR), evaluating target trafficking and elimination in tissue culture and in murine tumors. The work complies with all relevant ethical regulations. Cyclera Therapeutics oversaw compliance with biosafety regulations for in vitro work. Animal work compliance described in the pharmacokinetics and tumor implantation sections below.

Recombinant proteins, antibodies, and co-stains/secondary antibodies

Identities of catalog item recombinant proteins and antibodies can be found in the Supplementary Information.

EGF variant design using Rosetta

A previously-published co-crystal structure containing EGF and EGFR (PDB 1IVO) was processed to separate EGF (chain C) and EGFR domain III (chain A, residues 311-510). They were combined into a single PDB, which was used as the input for Rosettascripts[40] using proprietary XML scripts optimized for CDP redesign. 1000 unique variants were designed and scored using an interface analysis script, with 488 that had favorable scoring parameters incorporated into a mammalian surface display screening library. The steps for screening the binders and selectively mutagenizing the variants to identify a dominant-negative variant for CYpHER incorporation can be found in the Supplementary Information.

Mammalian surface display

Surface display flow cytometry was based on previously described protocols (62), with details found in Supplementary Information. The library screens for identifying and maturing EGFR-binding nanobody and EGF variants were each conducted once.

Recombinant protein production and analysis

Pilot CYpHER (Supplementary Fig. 1) molecule was produced as previously described[27]; in short, 293 FreeStyle cells (Thermo Fisher R79007) were transduced with constructs driving expression of the protein of interest at a multiplicity of infection ≈10 and grown until terminal volume (~30 mL) in FreeStyle 293 Expression Medium (Invitrogen 12338018) until harvest, 0.22-µm sterile filtration, and IMAC Ni-affinity chromatography (Cytiva, 17525501) purification. All other CYpHER molecules were produced by transient expression in suspension HEK293 cells (ThermoFisher GeneArt) and purified either via Ni-NTA pull-down as previously described[27] or by Protein A columns (Cytiva 28985254 [pre-packed Protein A columns] and 28903059 [buffer kit]) as per manufacturer's protocol. Proteins were buffer exchanged (Sephadex G25 desalting columns, Cytiva 17085101) into PBS and aliquoted for storage at −80 °C. SDS-PAGE (4–12% Bis-Tris 1 mm thickness, ThermoFisher NP0321BOX or NP0323BOX) was run with MES buffer (ThermoFisher NP0002) at 180 V for 50 min prior to Coomassie stain. SE-HPLC was performed on Agilent instrumentation using a TSKgel G3000SWXL column (Tosoh 08541). Mobile phase was 50 mM acetate pH 5.0, 100 mM NaCl, 100 mM arginine, 5% EtOH. Flow rate for the run was 0.5 mL/min. 100 µg protein was loaded.

Surface plasmon resonance (SPR) interaction analyses, microscopy, western blotting, cell viability dose response testing, immunohistochemistry, and ELISA

The details for the SPR, microscopy, Western blotting, cell viability dose response tests, immunohistochemistry, and ELISA can be found in the Supplementary Information.

Cancer cell line and primary keratinocyte surface protein flow cytometry

Detailed protocols can be found in the Supplementary Information. In brief, cells for surface protein analysis were lifted, pelleted, and stained for 30 min on ice with 10 nM of the appropriate antibody (anti-PD-L1, anti-EGFR, anti-TfR, or anti-human Fc), all of which were chosen to bind a site non-competitive with the CYpHER binding site. Fluorescent co-stains were included, permitting flow cytometry quantitation of surface protein after cells were rinsed. Note: where Y axes in figures are denoted with "vs PBS", "vs Untreated", or "vs No CYpHER", it means values were normalized to the mean of that sample (PBS, Untreated, or No CYpHER) prior to plotting.

Catalytic soluble protein uptake

The detailed protocol is available in the Supplementary Information. In brief, cells in 24 well plates were treated for 2 h with 20 nM biotinylated EGFRvIII with or without 5 nM CYpHER. After 2 h, cells were rinsed twice with PBS and then exposed to 10 nM biotinylated EGFRvIII and 10 nM iFluor 647-conjugated monovalent streptavidin. After 24 h, cells were lifted and analyzed by flow cytometry for fluorescence in the 647 channel, normalizing averages of cells treated with both EGFRvIII and CYpHER in Step 1 to cells only treated with EGFRvIII in Step 1.

In vivo pharmacokinetic analysis

PK work was performed at Charles River Laboratories with approval from their internal review board. For each test article, 12 female NCr nu/nu mice (8–10 weeks of age) received single IV doses of 1.5 mg/kg test article in PBS (or only PBS vehicle). Females were used for ease in re-housing and to reduce waste in the breeding scheme (males used for strain maintenance). Further development experiments will use both male and female mice. In groups of 3, mice were bled at 10 min, 30 min, 1 h, 2 h, 4 h, 8 h, 24 h, 48 h, 96 h, and 168 h. 12 mice produced these samples: one trio of mice was bled at 10 min, 4 h, and 96 h; one trio was bled at 30 min, 8 h, and 168 h; one trio was bled at 1 h and 24 h; and one trio was bled at 2 h and 48 h. Serum samples were snap-frozen and stored at −80 °C until analysis using an in-house ELISA method.

In vivo tumor implantation and dosage

Tumor implantation and dosage was performed at Seattle Children's Research Institute. All mice were maintained in accordance with the

National Institutes of Health Guide for the Care of Laboratory Animals with approval from the Seattle Children's Research Institute, Institutional Animal Care and Use Committee (protocol ACUC00682). 7-week-old female Athymic Nude mice (Foxn1^{nu}) were purchased from Inotiv Laboratories (#069) and housed under specific pathogen free conditions. Females were used for ease in re-housing and to reduce waste in the breeding scheme (males used for strain maintenance). Further development experiments will use both male and female mice. NCI-H1975 lung tumor cells were purchased from ATCC (CRL-5908) and verified human pathogen and mycoplasma free. CYpHER proteins CT-1212-1, CT-1222-1, and CT-5212-3 were formulated in phosphate-sucrose buffer and confirmed to meet endotoxin specifications. 5×10^6 tumor cells in PBS were inoculated in the subcutaneous space on the right flank of seven weeks old mice. Study enrollment was done en mass on day 0, 21 days after tumor implantation when the average tumor volume per group was 275 mm^3. Six mice were randomly assigned to each treatment group, normalizing for equal starting tumor volume. Vehicle or therapeutic were administered as a 200 µL bolus via tail vein injection on days 0, 3, and 7. Tumor volume and body weight were recorded on days 0, 2, 4, and 7. The study ended on day 8. Mice were removed from the study early if ulcerations developed on the tumor surface. Tumors did not reach IACUC-determined maximal size (1500 mm^3). For blood counts, mice bearing H1975 xenografts were treated twice per week IV with CT-1212-1 or vehicle for four weeks. 48 h after the final dose, mice were euthanized and blood collected. Blood was kept on ice and shipped overnight to IDEXX BioAnalytics (West Sacramento, CA) for complete blood count (CBC) analysis. All mice were group-housed with unrestricted mobility and free access to food and water for the duration of study. The housing room is maintained at 68–79 °F with 30–70% relative humidity on a 12-h light dark cycle.

Statistics and reproducibility

All comparisons within a given plot or panel were performed simultaneously. Measurements involved distinct samples; the same sample was not measured repeatedly. No data were excluded from analyses. Flow cytometry and microscopy experiments were performed once or twice as described in figure legends; when once, the experiments were compared to similar, but not identical, experiments (e.g., same cell line and treatment but different timepoints) for reproducibility assessment before inclusion in the manuscript. In vitro growth suppression experiments were performed once (A431, H358, SW48) or twice (A549, H1975, H1650, primary keratinocytes); when twice, both datasets produced similar data so one was used in analysis. Experiments consisted of 8-9 concentrations dosed in triplicate to arrive at reported potencies, calculated using Graphpad Prism v10, details for which can be found in the Supplementary Information. All animals in both the PK and tumor xenograft studies were female. No statistical method was used to predetermine sample size. Investigators were blinded to test article identity for the PK study, while the tumor xenograft study was unblinded. For the tumor xenografts, enrollment was done when the average tumor volume per group was 275 mm^3, randomly assigning mice to each treatment group, normalizing for equal starting tumor volume. For the ELISA, all murine serum samples were measured at two dilutions (1:100 and 1:1000) in technical triplicate, using whichever dilution produced interpolated values closest to the middle of the linear portion of the ten-point standard curve (technical triplicate at all concentrations) as the actual values. Full information on statistical tests used, significance values, and N per sample, are found in the Supplementary Data.

Reporting summary

Further information on research design is available in the Nature Portfolio Reporting Summary linked to this article.

Data availability

All data associated with this study are present in the paper, Supplementary Information and Supplementary Data. Additional information and/or materials related to this study, including recombinant proteins and datasets, will be made available through a material transfer agreement upon request to the corresponding author. Source data are provided with this paper.

References

1. Chang, M. T. et al. Identifying transcriptional programs underlying cancer drug response with TraCe-seq. *Nat. Biotechnol.* **40**, 86–93 (2022).
2. Dai, W. et al. Cetuximab inhibits oral squamous cell carcinoma invasion and metastasis via degradation of epidermal growth factor receptor. *J. Oral. Pathol. Med.* **43**, 250–257 (2014).
3. Lu, Y. et al. Epidermal Growth Factor Receptor (EGFR) Ubiquitination as a Mechanism of Acquired Resistance Escaping Treatment by the Anti-EGFR Monoclonal Antibody Cetuximab. *Cancer Res.* **67**, 8240–8247 (2007).
4. Du, Z. & Lovly, C. M. Mechanisms of receptor tyrosine kinase activation in cancer. *Mol. Cancer* **17**, 58 (2018).
5. Abourehab, M. A. S., Alqahtani, A. M., Youssif, B. G. M. & Gouda, A. M. Globally Approved EGFR Inhibitors: Insights into Their Syntheses, Target Kinases, Biological Activities, Receptor Interactions, and Metabolism. *Molecules* **26**, 6677 (2021).
6. Tomasello, C. et al. Resistance to EGFR inhibitors in non-small cell lung cancer: Clinical management and future perspectives. *Crit. Rev. Oncol. Hematol.* **123**, 149–161 (2018).
7. Fu, K., Xie, F., Wang, F. & Fu, L. Therapeutic strategies for EGFR-mutated non-small cell lung cancer patients with osimertinib resistance. *J. Hematol. Oncol.* **15**, 173 (2022).
8. Reslan, L., Dalle, S. & Dumontet, C. Understanding and circumventing resistance to anticancer monoclonal antibodies. *mAbs* **1**, 222–229 (2009).
9. Wells, J. A. & Kumru, K. Extracellular targeted protein degradation: an emerging modality for drug discovery. *Nat. Rev. Drug Discov.* https://doi.org/10.1038/s41573-023-00833-z (2023).
10. Schapira, M., Calabrese, M. F., Bullock, A. N. & Crews, C. M. Targeted protein degradation: expanding the toolbox. *Nat. Rev. Drug Discov.* **18**, 949–963 (2019).
11. Cotton, A. D., Nguyen, D. P., Gramespacher, J. A., Seiple, I. B. & Wells, J. A. Development of Antibody-Based PROTACs for the Degradation of the Cell-Surface Immune Checkpoint Protein PD-L1. *J. Am. Chem. Soc.* **143**, 593–598 (2021).
12. Siepe, D. H., Picton, L. K. & Garcia, K. C. Receptor Elimination by E3 Ubiquitin Ligase Recruitment (REULR): A Targeted Protein Degradation Toolbox. *ACS Synth. Biol.* **12**, 1081–1093 (2023).
13. Banik, S. M. et al. Lysosome-targeting chimaeras for degradation of extracellular proteins. *Nature* **584**, 291–297 (2020).
14. Leusmann, S., Ménová, P., Shanin, E., Titz, A. & Rademacher, C. Glycomimetics for the inhibition and modulation of lectins. *Chem. Soc. Rev.* **52**, 3663–3740 (2023).
15. Pance, K. et al. Modular cytokine receptor-targeting chimeras for targeted degradation of cell surface and extracellular proteins. *Nat. Biotechnol.* **41**, 273–281 (2023).
16. Mayle, K. M., Le, A. M. & Kamei, D. T. The intracellular trafficking pathway of transferrin. *Biochim. Biophys. Acta Gen. Subj.* **1820**, 264–281 (2012).
17. Jonker, C. T. H. et al. Accurate measurement of fast endocytic recycling kinetics in real time. *J. Cell Sci.* jcs.231225, https://doi.org/10.1242/jcs.231225 (2019).
18. Awuah, P., Bera, T. K., Folivi, M., Chertov, O. & Pastan, I. Reduced Shedding of Surface Mesothelin Improves Efficacy of Mesothelin-Targeting Recombinant Immunotoxins. *Mol. Cancer Therapeutics* **15**, 1648–1655 (2016).

19. Essaghir, A. & Demoulin, J.-B. A Minimal Connected Network of Transcription Factors Regulated in Human Tumors and Its Application to the Quest for Universal Cancer Biomarkers. *PLoS ONE* **7**, e39666 (2012).
20. Shen, Y. et al. Transferrin receptor 1 in cancer: a new sight for cancer therapy. *Am. J. Cancer Res* **8**, 916–931 (2018).
21. Rahman, S. A., Yokoyama, M., Nishio, S. & Takeuchi, M. Flow cytometric evaluation of transferrin receptor in transitional cell carcinoma. *Urol. Res.* **25**, 325–329 (1997).
22. Meyers, R. M. et al. Computational correction of copy number effect improves specificity of CRISPR–Cas9 essentiality screens in cancer cells. *Nat. Genet* **49**, 1779–1784 (2017).
23. Johnsen, K. B., Burkhart, A., Thomsen, L. B., Andresen, T. L. & Moos, T. Targeting the transferrin receptor for brain drug delivery. *Prog. Neurobiol.* **181**, 101665 (2019).
24. Kariolis, M. S. et al. Brain delivery of therapeutic proteins using an Fc fragment blood-brain barrier transport vehicle in mice and monkeys. *Sci. Transl. Med.* **12**, eaay1359 (2020).
25. Crook, Z. R. et al. A TfR-Binding Cystine-Dense Peptide Promotes Blood–Brain Barrier Penetration of Bioactive Molecules. *J. Mol. Biol.* **432**, 3989–4009 (2020).
26. Zhang, D. et al. *Transferrin Receptor Targeting Chimeras (TransTACs) for Membrane Protein Degradation*. http://biorxiv.org/lookup/doi/10.1101/2023.08.10.552782, https://doi.org/10.1101/2023.08.10.552782 (2023).
27. Crook, Z. R. et al. Ex silico engineering of cystine-dense peptides yielding a potent bispecific T cell engager. *Sci. Transl. Med.* **14**, eabn0402 (2022).
28. Crook, Z. R., Sevilla, G. P., Mhyre, A. J. & Olson, J. M. Mammalian Surface Display Screening of Diverse Cystine-Dense Peptide Libraries for Difficult-to-Drug Targets. In *Genotype Phenotype Coupling* (eds. Zielonka, S. & Krah, S.) vol. 2070 363–396 (Springer US, 2020).
29. Lawson, N. L. et al. Mapping the binding sites of antibodies utilized in programmed cell death ligand-1 predictive immunohistochemical assays for use with immuno-oncology therapies. *Mod. Pathol.* **33**, 518–530 (2020).
30. Thomas, R. & Weihua, Z. Rethink of EGFR in Cancer With Its Kinase Independent Function on Board. *Front. Oncol.* **9**, 800 (2019).
31. Troiani, T. et al. Therapeutic value of EGFR inhibition in CRC and NSCLC: 15 years of clinical evidence. *ESMO Open* **1**, e000088 (2016).
32. Eskilsson, E. et al. EGFR heterogeneity and implications for therapeutic intervention in glioblastoma. *Neuro Oncol.* **20**, 743–752 (2018).
33. Boeckx, C. et al. Anti-Epidermal Growth Factor Receptor Therapy in Head and Neck Squamous Cell Carcinoma: Focus on Potential Molecular Mechanisms of Drug Resistance. *Oncologist* **18**, 850–864 (2013).
34. Passaro, A., Jänne, P. A., Mok, T. & Peters, S. Overcoming therapy resistance in EGFR-mutant lung cancer. *Nat. Cancer* **2**, 377–391 (2021).
35. Weihua, Z. et al. Survival of Cancer Cells Is Maintained by EGFR Independent of Its Kinase Activity. *Cancer Cell* **13**, 385–393 (2008).
36. Katreddy, R. R. et al. Targeted reduction of the EGFR protein, but not inhibition of its kinase activity, induces mitophagy and death of cancer cells through activation of mTORC2 and Akt. *Oncogenesis* **7**, 5 (2018).
37. Roovers, R. C. et al. Efficient inhibition of EGFR signalling and of tumour growth by antagonistic anti-EGFR Nanobodies. *Cancer Immunol. Immunother.* **56**, 303–317 (2007).
38. Schmitz, K. R., Bagchi, A., Roovers, R. C., van Bergen en Henegouwen, P. M. P. & Ferguson, K. M. Structural Evaluation of EGFR Inhibition Mechanisms for Nanobodies/VHH Domains. *Structure* **21**, 1214–1224 (2013).
39. French, A. R., Tadaki, D. K., Niyogi, S. K. & Lauffenburger, D. A. Intracellular Trafficking of Epidermal Growth Factor Family Ligands Is Directly Influenced by the pH Sensitivity of the Receptor/Ligand Interaction. *J. Biol. Chem.* **270**, 4334–4340 (1995).
40. Fleishman, S. J. et al. RosettaScripts: A Scripting Language Interface to the Rosetta Macromolecular Modeling Suite. *PLoS One* **6**, e20161 (2011).
41. Leaver-Fay, A. et al. Rosetta3. in *Methods in Enzymology* vol. 487, 545–574 (Elsevier, 2011).
42. Ogiso, H. et al. Crystal Structure of the Complex of Human Epidermal Growth Factor and Receptor Extracellular Domains. *Cell* **110**, 775–787 (2002).
43. Cochran, J. R., Kim, Y.-S., Olsen, M. J., Bhandari, R. & Wittrup, K. D. Domain-level antibody epitope mapping through yeast surface display of epidermal growth factor receptor fragments. *J. Immunological Methods* **287**, 147–158 (2004).
44. Ahn, G. et al. Elucidating the cellular determinants of targeted membrane protein degradation by lysosome-targeting chimeras. *Science* **382**, eadf6249 (2023).
45. Panaccio, M. et al. Heterogeneity of the human transferrin receptor and use of anti-transferrin receptor antibodies to detect tumours in vivo. *Immunol. Cell Biol.* **65**, 461–472 (1987).
46. Greig, M. J. et al. Effects of Activating Mutations on EGFR Cellular Protein Turnover and Amino Acid Recycling Determined Using SILAC Mass Spectrometry. *Int. J. Cell Biol.* **2015**, 1–8 (2015).
47. Niewoehner, J. et al. Increased Brain Penetration and Potency of a Therapeutic Antibody Using a Monovalent Molecular Shuttle. *Neuron* **81**, 49–60 (2014).
48. Chamberlain, P. P. & Hamann, L. G. Development of targeted protein degradation therapeutics. *Nat. Chem. Biol.* **15**, 937–944 (2019).
49. Cross, D. A. E. et al. AZD9291, an Irreversible EGFR TKI, Overcomes T790M-Mediated Resistance to EGFR Inhibitors in Lung Cancer. *Cancer Discov.* **4**, 1046–1061 (2014).
50. Pinilla-Macua, I., Grassart, A., Duvvuri, U., Watkins, S. C. & Sorkin, A. EGF receptor signaling, phosphorylation, ubiquitylation and endocytosis in tumors in vivo. *eLife* **6**, e31993 (2017).
51. Yuan, Z. et al. An A13 Repeat within the 3′-Untranslated Region of Epidermal Growth Factor Receptor (EGFR) Is Frequently Mutated in Microsatellite Instability Colon Cancers and Is Associated with Increased EGFR Expression. *Cancer Res.* **69**, 7811–7818 (2009).
52. Ashraf, S. Q. et al. Direct and immune mediated antibody targeting of *ERBB* receptors in a colorectal cancer cell-line panel. *Proc. Natl Acad. Sci. USA* **109**, 21046–21051 (2012).
53. Morris, V. K. et al. Treatment of Metastatic Colorectal Cancer: ASCO Guideline. *JCO* **41**, 678–700 (2023).
54. Pastore, S., Lulli, D. & Girolomoni, G. Epidermal growth factor receptor signalling in keratinocyte biology: implications for skin toxicity of tyrosine kinase inhibitors. *Arch. Toxicol.* **88**, 1189–1203 (2014).
55. Couch, J. A. et al. Addressing Safety Liabilities of TfR Bispecific Antibodies That Cross the Blood-Brain Barrier. *Sci. Transl. Med.* **5**, 183ra57 (2013).
56. Ogama, Y. et al. Phase 1 Clinical Trial of PPMX-T003, a Novel Human Monoclonal Antibody Specific for Transferrin Receptor 1, to Evaluate Its Safety, Pharmacokinetics, and Pharmacodynamics. *Clin. Pharm. Drug Dev.* **12**, 579–587 (2023).
57. Arguello, A. et al. Molecular architecture determines brain delivery of a transferrin receptor–targeted lysosomal enzyme. *J. Exp. Med.* **219**, e20211057 (2022).

Acknowledgements

The authors wish to thank Pauline Bariola and Jacob Felcyn for development of the SE-HPLC methodology, Jeannette Bannink for help with ELISA development and PK data interpretation and analysis, Akinsola Oyelakin for help with tissue processing, Andrew J. Mhyre for in vivo

study discussions, and Connor Burns for slide scanning. Figures 1A, B, 2B, 3D, 6A, 8C, and Supplementary Fig. 1A were created with Biorender. The project was supported by NIH grant R01 CA223674 (to J.M.O.); Run of Hope; Project Violet; Seattle Children's Research Institute startup funds; Blaze Bioscience, Inc; and Cyclera Therapeutics, Inc.

Author contributions

Z.R.C., J.P., J.M.O, and N.W.N. conceptualized the research. Z.R.C., G.P.S., P.Y., E.J.G., T-D.P., and M.H. designed the experiments. Z.R.C., G.P.S., P.Y., E.J.G., T-D.P., and M.L.H. performed the experiments and/or contributed to data analysis. Z.R.C. and M.L.H. produced figures. J.M.O. and N.W.N. contributed to funding acquisition. Z.R.C., G.P.S., E.J.G., J.M.O., and N.W.N. supervised researchers. Z.R.C., E.J.G., M.L.H., J.M.O., and N.W.N. wrote the manuscript. All authors contributed to review of the manuscript.

Competing interests

Cyclera Therapeutics Inc. retains intellectual property rights to the technology described in this manuscript. Z.R.C., G.P.S., and N.W.N. own stock in and are or were employees of Cyclera. J.M.O. owns stock in and is an advisor of Cyclera. Z.R.C., J.M.O., and N.W.N. are inventors on patent applications for this technology. Z.R.C., G.P.S., P.Y., T-D.P., and N.W.N were previously employees of Blaze and may own stock in Blaze. E.J.G., M.L.H., and J.P. have no competing interests.

Additional information

Supplementary information The online version contains supplementary material available at https://doi.org/10.1038/s41467-024-52975-2.

Correspondence and requests for materials should be addressed to Natalie W. Nairn.

Peer review information *Nature Communications* thanks Sonia Levi, who co-reviewed with Andrea MoroQiwei Wang and the other, anonymous, reviewer(s) for their contribution to the peer review of this work. A peer review file is available.